Journal of Inorganic and Organometallic Polymers and Materials
https://doi.org/10.1007/s10904-026-04176-1

RESEARCH

PVDF-TiO_2-nZVI Nanocomposite Membranes for the Remediation of Heavy Metal Contaminated Wastewater

Murtala Namakka[1,2] · Md. Rezaur Rahman[1] · Khairul Anwar Bin Mohamed Said[1] · Bavya Devi Karuppasamy[3] · Aliyu Abubakar Shehu[4]

Received: 6 December 2025 / Accepted: 6 January 2026

Abstract

Heavy metal pollution poses a significant threat to environmental and human health. Despite recent advancements in nanofiltration technologies, further innovations are essential to optimize both the heavy metal removal efficiency and hydraulic performance of the nanocomposite membranes. Herein, A TiO_2-nZVI nanocomposite was synthesized by impregnating titania (TiO_2) with nano zero valent iron (nZVI) via chemical reduction method and subsequently integrated into polyvinylidene fluoride (PVDF) membranes via phase inversion technique. Five distinct membrane configurations were fabricated by varying the nanocomposite loadings. The physicochemical properties of the nanocomposite performance of these membranes were evaluated via various characterization techniques including FESEM, FTIR, EDX, XRD, XPS, TGA, water contact angle, solvent content analysis, pure water flux and Pb^{2+} removal. The optimal PVDF-TiO_2-nZVI membrane was determined via detailed performance evaluation at 10ppm Pb^{2+} concentration. Influence of concentration on optimum membrane performance was investigated by varying Pb^{2+} concentrations. The removal efficiencies of the PVDF- TiO_2-nZVI membranes were found consistent (> 80% across all membranes) with optimum membrane (A4) achieving 91% Pb^{2+} removal with a sustained hydraulic property during the filtration operation.

Graphical Abstract

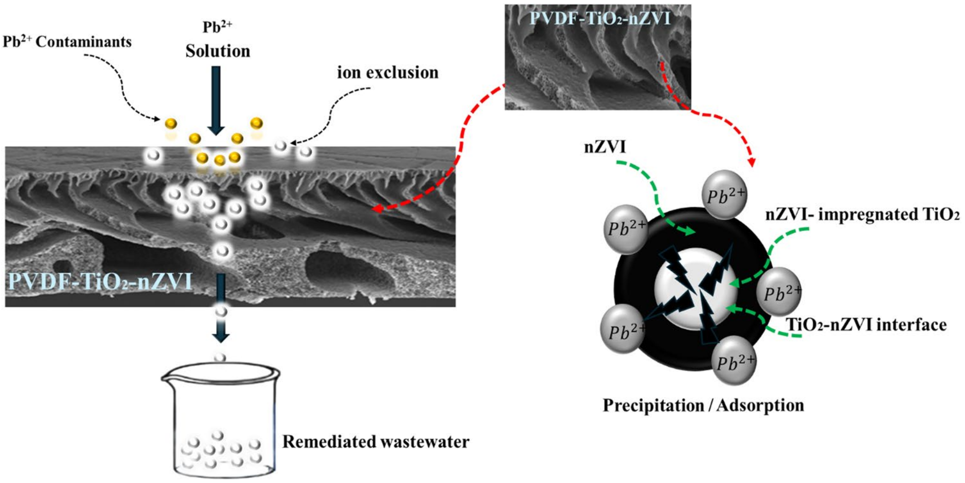

Keywords Nanocomposite membrane · Hydrophilicity · Nanocomposite · Nanoparticle · Zero valent iron · Heav-metals removal

---

Extended author information available on the last page of the article

1 Introduction

Heavy metal pollution is a contemporary environmental challenge (Abdelsalam et al. 2024) associated with the discharge of heavy metals into water systems. Recent research has examined the detrimental effects of heavy metal contaminants such as chromium (Khedawy et al. 2025), lead (Pb^{2+}) (L. Zhang et al. 2024a, b, c), cadmium (Zhang et al. 2024a, b, c), and Arsenic (An et al. 2025) on both ecological and human health. Despite the remediation efforts, heavy metal contamination remains a significant concern. One of the most common heavy metal contaminants is Pb^{2+} contamination and has been reported to affect humans (El-Said et al. 2024) and ecosystem due to its high toxicity (Abdelmoaty et al. 2022). This cumulative neurotoxicant leaches from several sources including mining sites and aging infrastructures. Paediatric exposure to Pb^{2+} causes irreversible neurocognitive damage, while chronic adult exposure elevates risks of cardiovascular and renal disease (Yu 2025). The nature of Pb^{2+} contamination which proves to persist despite regulations (Schneider 2023), and demands highly efficient point-of-use technologies capable of ultra-low-level removal. Hence, the development of advance materials and strategies for the removal of Pb^{2+} contaminants are essential in mitigating these potential health hazards and future environmental contaminations. Conventional methods such as chemical precipitation (Benalia et al. 2022; Chen et al. 2009), ion exchange (Jasim And Ajjam 2024; Sgreccia et al. 2024), electrochemical (Okpara et al. 2022; Wang et al. 2022) and adsorption (El-Sadaawy et al. 2025; Shaker et al. 2025) are commonly employed with relative success.

However, limitations such as selectivity in ion exchange, resin production, and the formation of passive non-conductive layers in electrochemical methods inspired researchers in developing alternative approaches. Recently, Zhang et al., highlighted the limitations and challenges associated with surface-modified nanostructured adsorbents, such as high cost, low stability, poor scalability, and potential nanotoxicity (X. Zhang et al. 2024a, b, c). As a result, advanced oxidation processes combined with other wastewater treatment strategies have been investigated to improve target ion selectivity while ensuring a stable adsorption capacity (Khader et al. 2024; Yan et al. 2024). Nevertheless, long operation time (Munawar et al. 2024), excessive sludge formation (Fatta-Kassinos et al. 2011), remains a challenge in adopting these strategies, making the adsorption the most widely employed strategy (He et al. 2025).The effectiveness of the adsorption method is essentially dependent on the characteristics and catalytic activity of the adsorbent. Nano zero valent iron (nZVI) is characterized by its exceptional reactivity, injective ability and large surface area electron donor that reduces emerging contaminants (Zafar et al. 2024). However, individual nZVI particles can easily passivate or agglomerate thereby limiting overall performance (Minella et al. 2016). Researchers have reported enhanced stability of nZVI by incorporating nZVI with support materials forming stable nanocomposite with less potential passivation properties shielding active nZVI surface particularly titania, TiO_2 (Brossault et al. 2021), an adsorbent capable of mineralizing heavy metal contaminants. Prior studies have shown nZVI and TiO_2 based adsorbents exhibiting a higher capacity for Pb^{2+} adsorption. Mensah et al. demonstrated the effectiveness of TiO_2-nZVI nanocomposite for wastewater treatment through efficient adsorption of heavy metals including Pb^{2+} (Mensah et al. 2023). In a similar study, magnetic TiO_2-nZVI nanoparticles were reported to possess excellent potential for the electrochemical detection of dopamine (Qureashi et al. 2024a). However, in addition to post treatment, this approach faces challenges related to unstable adsorption efficiency (Jing et al. 2023).

To address this challenge, it is crucial to develop effective and sustainable remediation approach capable of preventing formation of passive layers and nanomaterial aggregation while efficiently combating the diverse range of toxic heavy metals from wastewater effluents (Chowdhury et al. 2022). Polyvinylidene fluoride (PVDF) membranes, known for their excellent mechanical properties, chemical stability, and diverse applications, have been extensively studied (Awasthi et al. 2023; Khan et al., 2025; Tofighy et al. 2021). However, their inherent limitations, such as low permeability and fouling propensity, necessitate the development of advanced composite membranes. A promising approach to enhance the performance of PVDF membranes involves the incorporation of nanoparticles, which can significantly improve separation efficiency and functionality (Prabhakar et al. 2024). Krishnan et al. investigated the immobilization of nZVI on a PVDF membrane by surface modification with polyacrylic acid (PAA), performance of the developed PVDF-nZVI membrane revealed excellent reductive decolorization of azo dye (Krishnan et al. 2023). The incorporation of TiO_2 nanoparticles into PVDF membranes is reported to enhance hydrophilicity, improve antifouling performance, and impart photocatalytic self-cleaning capabilities to PVDF membranes (Le et al. 2023; Ong et al. 2014). While PVDF-TiO_2 modified membranes have demonstrated significant potential for wastewater remediation via adsorption, the mechanism of these membranes is predominantly photocatalytic oxidation, which is less effective for the complete and rapid removal of non-degradable heavy metal ions that require a strong reductive process.

PVDF-nZVI membranes possess excellent reductive capacity but often suffer from nZVI oxidation, compromising long-term stability. The synergistic combination of nZVI and TiO_2 forms effective nanocomposite membranes which reduce the recombination of particles electron-hole pairs. In this study, a TiO_2-nZVI nanocomposite with distinct properties and enhanced adsorption capacities was synthesized via chemical reduction method. Subsequently, the nanocomposite was incorporated into a PVDF matrix at precise loadings (0.1, 0.15, 0.2, 0.25, and 0.3 g) to fabricate a series of PVDF-TiO_2-nZVI nanocomposite membranes (designated A1-A5) via the phase-inversion technique, with a pristine PVDF membrane (A0) serving as the control membrane. The structural, morphological, and surface characteristics of the fabricated membranes were characterized using various analytical techniques. Performance of the PVDF-TiO_2-nZVI nanocomposite membranes were assessed via metrics including solvent content, hydrophilicity, water flux and efficiency in the remediation of aqueous Pb^{2+} at various concentrations.

2 Materials and methods

2.1 Materials

For the fabrication of TiO_2-nZVI nanocomposite, all procured Chemicals including Sodium borohydride, $NaBH_4$, Iro sulfate heptahydrate, $FeSO_4{\cdot}7H_2O$, Ethanol, CH_3CH_2OH, Methanol CH_3OH, Sodium Hydroxide, NaOH, Hydrochloric Acid HCl, Titanium oxide TiO_2 (CAS No: 13463-67-7), were used as procured from Sigma-Aldrich Sdn. Bhd. (Malaysia). Chemicals for nanocomposite membrane fabrication includes Poly vinylidene fluoride, (PVDF) (CAS No: 24937-79-9, Mm 534,000 g mol^{-1}) as the primary polymer matrix for its intrinsic chemical resistivity and thermal stability, N-Methyl-2-pyrrolidone (NMP) as a solvent to ensure a homogeneous dispersion of TiO_2-nZVI nanoparticles in the casting solution. Throughout the experimental procedures, all aqueous reagent solutions were prepared with ultrapure water while industrial grade nitrogen gas, N_2 utilized in this work, was provided by Universiti of Malysia Sarawak.

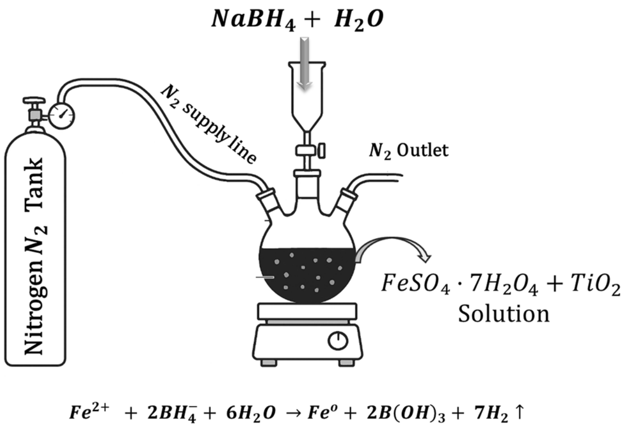

Fig. 1 Schematic diagram of TiO_2-nZVI nanoparticle synthesis

2.2 Synthesis of TiO_2-nZVI Nanoparticles

The TiO_2-nZVI nanocomposite was synthesized following the procedure described in (Namakka et al., 2024a) and (Hejri et al. 2019) with little modifications. Briefly, a precursor solution was prepared by dissolving 5.56 g of ferrous sulfate heptahydrate ($FeSO_4{\cdot}7\ H_2O$) and a specific amount of pre-synthesized TiO_2 nanoparticles in 200 mL of ultrapure water within a three-necked flask (See Fig. 1). The mixture was continuously purged with N_2 gas under constant stirring for 30 min to achieve a homogeneous, oxygen-free TiO_2-$FeSO_4$ solution. Sodium hydroxide (NaOH) and hydrochloric acid (HCl) (0.01 mol L^{-1}) were used to adjust the solution pH. Concurrently, sodium borohydride ($NaBH_4$) reducing agent solution was formulated by dissolving 1.60 g of $NaBH_4$ in 50mL deionized water.

The reduction of ferrous ions, Fe^{2+} to zero valent iron Fe^0 on the TiO_2 particles was subsequently initiated by the dropwise addition of the $NaBH_4$ solution into the TiO_2-$FeSO_4$ solution (See Eqs. 1–3).

$$FeSO_4.7H_2O + 2NaBH_4 \rightarrow Fe^o + NaSO_4 + 7H_2O + 2B(OH)_3 \qquad (1)$$

$$Fe^{2+} + 2BH_4^- + 6H_2O \rightarrow Fe^o + 2B(OH)_3 + 7H_2\uparrow \qquad (2)$$

$$Fe^{2+} + 2e^- \rightarrow Fe^O \qquad (3)$$

The reaction was allowed to proceed for 25 min; the cessation of gas evolution and complete formation of black colored particles indicates quantitative reduction of Fe^{2+} to Fe^0. The solution was allowed to settle for few minutes, washed several times using 95% ethanol to remove excess reactants and uncoated TiO_2 particles before centrifuging for 5 min at 20,000 revolution per minute at room temperature. The binary composite was dried at 90 °C for 4 h in a tube furnace under nitrogen condition. Dried TiO_2-nZVI nanoparticles were stored for further characterizations.

2.3 Fabrication of PVDF-TiO_2-nZVI Nanocomposite Membranes

Polyvinylidene fluoride (PVDF) and NMP were used as the base polymer and PVDF solvent for the preparation of dope solutions, while synthesized TiO_2-nZVI nanoparticles were incorporated into the membrane dope solution to enhance hydrophilicity, self-cleaning and overall performance of the nanocomposite membrane. The dope solutions were prepared following the procedure described in(Nawaz et al.

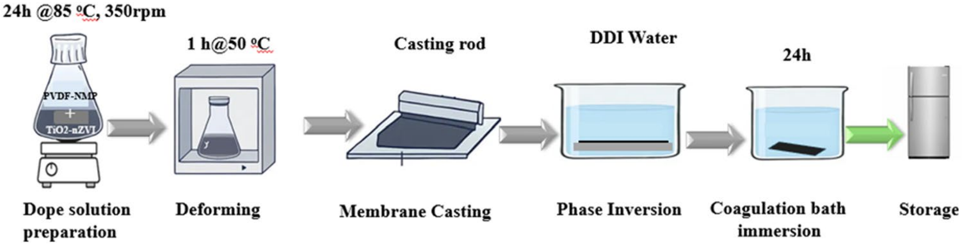

Fig. 2 Schematic set up of PVD-TiO_2-nZVI nanocomposite membranes fabrication

Table 1 Code and compositions of fabricated TiO_2-nZVI nanocomposite membranes

Code	PVDF (wt%)	Concentration of TiO_2-nZVI (grams)	NMP Solvent (v%)
Ao	14	0	86
A1	14	0.10	86
A2	14	0.15	86
A3	14	0.20	86
A4	14	0.25	86
A5	14	0.30	86

2021) and (R. Rahman et al. 2024a, b) with the following modifications (see Fig. 2).

Briefly, PVDF pellets (14% w/v) were added to a predetermined volume of NMP solvent in a 250 ml conical flask. TiO_2-nZVI nanoparticles were subsequently introduced at varying concentrations viz. 0.1 g, 0.15 g, 0.20 g, 0.25 g and 0.30 g. The solutions were covered using foil paper and subjected to 350 rpm magnetic stirring at 85 °C for 24 h to ensure effective dissolution and homogenous dispersion of the TiO_2-nZVI nanoparticles in the dope solutions. To eliminate possibly entrapped air bubbles introduced during stirring, which could potentially introduce defects in the cast membrane, the homogenously dispersed dope solutions were transferred to an oven and held at 50 °C for 1 h, this procedure reduces the solution viscosity and allows microbubbles to coalesce. Subsequently, the bubble-free dope solution (approximately 10 ml) was cast onto a clean, dry glass substrate (21 cm × 30 cm) using a doctor blade film applicator and immediately immersed in a coagulation bath containing deionized water maintained at room temperature (approximately 25 °C). This step helps initiate the non-solvent induced phase separation process, resulting in the solidification of the polymer solution and the formation of a hydrophilic TiO_2-nZVI nanocomposite membrane. Following phase inversion, the nanocomposite membranes were transferred to another coagulation bath containing fresh deionized water for 12 h (overnight). The coagulation bath water was replaced with fresh distilled water to ensure the complete extraction of residual NMP solvent and any soluble components from the TiO_2-nZVI nanocomposite membrane matrix. Finally, the nanocomposite membranes were stored in a fridge for further analysis. Table 1 shows the TiO_2-nZVI nanocomposite membrane designated code and compositions.

2.4 Characterizations

Synthesized TiO_2-nZVI and the fabricated nanocomposite membranes were characterized via X-ray diffraction, XRD, Fourier-transform infrared, FTIR, Thermal gravimetric analysis, TGA, Field emission scanning electron microscopy coupled with energy-dispersive X-ray spectroscopy FESEM/EDS, and X-ray Photoelectron Spectroscopy, XPS analytical techniques to corroborate the physicochemical properties and chemical bonding of the synthesised nanocomposite material. FTIR spectroscopy was performed using a Shimadzu IRAffinity-1 spectrometer to characterize the molecular bond structures and functional groups of the nanoparticles and the fabricated membranes. Both analyses were conducted in attenuated total reflectance (ATR) mode across a wavenumber range of 4000 to 400 cm^{-1}, with a spectral resolution of 4 cm^{-1} and an accumulation of 32 scans per spectrum. For measurement, a section of each sample was placed on the ATR crystal and secured with a swivel press to ensure optimal surface contact.

The surface morphology and elemental composition of the synthesized nanocomposites were characterized using FESEM-EDS, which are well-established techniques for microstructural and elemental analysis (Aziz And Abdel-Karim 2023; Sharma et al. 2019). The FESEM images (x20000 and x50,000 magnification) were acquired with a Hitachi S-4700 instrument, operating at an accelerating voltage of 20 kV, which illustrates the morphological structure of the TiO_2-nZVI nanocomposites and modified PVDF-TiO_2-nZVI nanocomposite membranes. Subsequently, the thermal stability of the TiO_2-nZVI and the physicochemical properties of the synthesized TiO_2-nZVI nanocomposite material was evaluated via TGA analysis under the following conditions: on set temperature of 323.69 °C, Inflect. Point temperature 372.92 °C, End set temperature 388.95 °C and Midpoint 351.52 °C under constant N_2 supply.

XPS analysis was conducted to investigate the chemical bonding and elemental interactions within the nanocomposite material. The analysis followed the procedure described in (Baily et al., n.d.; Major et al. 2022) and the deconvolutions and peaks identification were guided by the standard procedure described in ThermoFisher scientific. The analysis was carried out in Alpha-K XPS spectrometer using monochromatic aluminium radiation at 0.3 eV FWHM,1.5% pass energy resolution and 11.75 eV to 23.5 eV measurement pass energy resolution as described in operation manual. The crystallinity and phase composition of the TiO_2-nZVI nanoparticles and the fabricated nanocomposite membranes were analysed using XRD. Measurements were performed at ambient temperature on a Rigaku SmartLab Powder X-ray diffractometer. Data were collected over a 2θ angular range from 0° to 80°. The crystalline index (CrI), serving as a measure of the degree of crystallinity, was determined using the empirical equations described in (James et al. 2024a).

$$\text{Crystalline index } (\%) = \frac{A_c}{A_t} \times 100 \tag{4}$$

$$A_t = A_C + A_m \tag{5}$$

$$D = \frac{k\lambda}{\beta \cos\theta} \tag{6}$$

where.

Ac represent “Area of all the crystalline peak.

A_m represents the area of amorphous peaks.

A_t total area of all peaks.

k is the Scherrer constant = 0.94.

λ (nm) is the X-ray wavelength = 1.5418.

β (radians) represent the full width at half maximum, FWHM.

θ (Degree) is the Bragg angle.

2.5 Nanocomposite Membrane Performance Analysis

2.5.1 Membrane Porosity

The porosity of the TiO_2-nZVI nanocomposite membranes was measured by recording the weight of the membrane piece before and after wetting. The wetted membrane was immersed in deionized water for 24 h as described in (M. R. Rahman et al., 2025a). The porosity was evaluated following Eq. 7 described below.

$$\varepsilon\ (\%) = \frac{\left(\frac{Wa - Wb}{\rho w}\right)}{\left(\frac{Wa - Wb}{\rho w}\right) + \left(\frac{Wb}{\rho PVDF}\right)} \times 100 \tag{7}$$

Where,

w_a and w_b are the weight of wet and dry membrane (g);

ρ_w and ρ_{PVDF} are the density of water (0.998 g/cm^3) and PVDF polymer (1.740 g/cm^3).

2.5.2 Membrane Hydrophilicity

The surface hydrophilicity of the fabricated TiO_2-nZVI membranes was quantitatively evaluated through static water contact angle, WCA measurements, employing the sessile drop method with an Ossila contact angle goniometer. Ultrapure water was used as the probe liquid (Hurwitz et al. 2010a). To ensure surface heterogeneity, measurements were repeated randomly in three different selected locations per sample. Influence of time on the water contact angle was evaluated. The reported contact angle value represents the arithmetic mean of these replicate measurements, providing a robust characterization of the macroscopic wetting characteristics.

2.5.3 Membrane Solvent Content Analysis

The solvent uptake behavior and swelling characteristics of the TiO_2-nZVI nanocomposite membrane were quantitatively analyzed to investigate the thermodynamic interactions between the polymer matrix and other polar solvents viz. water, ethanol and methanol. Briefly, a piece of the TiO_2-nZVI nanocomposite membrane with a uniform area of 1 cm² was cut and immersed in water, methanol and ethanol for 24 h until equilibrium swelling was achieved, the weight of the membrane before and after wetting were measured. This approach was utilized by (Iqbal et al. 2019) and (Nawaz et al. 2021). The procedure was repeated for each of the three replicates. The degree of swelling was assessed gravimetrically by calculating the mass difference between the swollen equilibrated state, W_s and the dry state W_d. The equilibrium solvent content (S_c), expressed as a percentage, was then determined by the following mathematical expression.

$$S_c = \frac{W_s - W_d}{W_s} \times 100 \tag{8}$$

2.5.4 Membrane Pure Water Flux Analysis

The methodology described in (Khui et al. 2025) was modified. Briefly, the nanocomposite membrane discs (4.4 cm diameter) were cut and installed in the filtration unit. After loading 2.5 L of pure water, the system was started at zero pressure. A stabilization period involved gradually increasing the pressure to 2.0 bars for 30 min. The system was then operated at 1.0 bar, with permeate volume measured at 5-minute intervals over 65 min. Water permeation flux was calculated as described by James et al., 2024. For accuracy, the experiment was replicated for each membrane, and average flux values were determined using the following Eq.

$$Pure\,Water\,Flux\ (J_w)\ =\ \frac{Q}{A\,\Delta T} \tag{10}$$

Where **Q** is the amount of pure water that passes the nanocomposite membrane (m^3), ΔT is the filtration time (**h**), **A** is the membrane area (m^2).

2.5.5 Nanocomposite Membrane Heavy Metal Removal Analysis

The heavy metal rejection performance of the nanocomposite membranes was evaluated with aqueous solutions of Pb^{2+} at varying concentrations. Initially, 10ppm single ion aqueous solutions of Pb^{2+} were prepared for the first filtration cycle for all the nanocomposite membranes (Ao, A1, A2, A3, A4 and A5) to determine the membrane with optimum performance. Subsequently, the optimum membrane was subjected to the varying Pb^{2+} concentrations (20ppm,30ppm and 40ppm) to evaluate the influence of heavy metal concentration on the overall nanocomposite membrane performance. Each of the filtration experiments were conducted at 1 bar and 25 °C for 70 min. Prior to testing, a preconditioning protocol described in water flux analysis was implemented, wherein the nanocomposite membrane was compacted at 2 bar for 20 min, followed by a 10-minute stabilization period with the heavy metal solution at the same pressure to ensure structural stability and prevent artificially high initial rejection values. The feed solution was refilled continuously to maintain consistent feed concentrations. The concentration of heavy metal ions in the permeate was analyzed using atomic absorption spectroscopy (AAS) calibrated with a standard curve. The heavy metal rejection rate (R) was determined according to the following equation (Razavi et al. 2025):

$$R\,(\%) = \left[1 - \left(\frac{Cp}{Cf}\right)\right] \times 100 \tag{11}$$

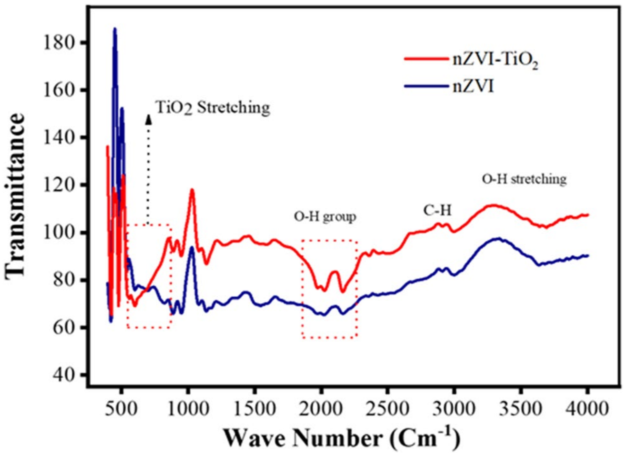

Fig. 3 FTIR of the synthesized nZVI and TiO_2-nZVI, nanoparticles

3 Results and Discussion

3.1 FTIR of nZVI, and TiO_2-nZVI Nanocomposite

Figure 3 shows the results from the FTIR with attenuated total reflectance (FTIR-ATR) employed to characterize the functional groups present in the synthesized nZVI, and nZVI-TiO_2. The spectra for nZVI and TiO_2-nZVI nanoparticles exhibited distinct characteristic absorption peaks correlated with the vibrational modes of their constituent chemical bonds. The FTIR spectra of the nZVI and nZVI impregnated TiO_2 nanoparticles were nearly identical, indicating that the composite is predominantly composed of the coated nZVI surface layer. In the FTIR spectrum of the TiO_2-nZVI composite, a broad absorption band observed at 3400.23 cm^{-1} is attributed to O-H stretching vibrations, which is consistent with the typical range for this functional group (M. R. Rahman et al., 2025b). The peaks at 1590.78 cm^{-1} and 2104 cm^{-1} collectively suggest the presence of O-H bonds associated with the formation of α-FeOOH (Namakka et al., 2024; R. Zhang et al. 2023a, b). Furthermore, a shift in the Ti-O-Ti stretching vibration absorption band from 720 cm^{-1} to a lower wavenumber of 516.09 cm^{-1} corroborate the successful compositional integration of nZVI in TiO_2 surface layer (Qureashi et al. 2024b). Consequently, the -OH tensile vibration peaks are observed at 2104 cm^{-1} and -OH stretching ~ 3400 cm^{-1}–3500 cm^{-1} with clear C-H vibrations around 2800 cm^{-1}, are influenced by the presence of TiO_2 components in the TiO_2-ZVI, nanoparticle thereby increasing the overall -OH functional group on the TiO_2-nZVI nanocomposite material.

The effective encapsulation of nZVI on TiO_2 matrix is essential for enhanced stability and reactivity. This enhanced catalytic activity of TiO_2-nZVI according to Hsieh et al. (2010) was attributed to the trapping of the electron generated on the TiO_2 surface via half reaction of $Fe^{3+/}Fe^{2+}$ thereby sustaining the catalytic activity of TiO_2 while preventing electron hole recombination of iron material. The findings further reinstated the anti-corrosion potential of nZVI impregnated TiO_2 nanocomposite compared to bare nZVI material, preventing rapid oxidation and sustaining the chemical reactivity of the nZVI (Hsieh et al. 2010). The nZVI outer surface passivation potential, particularly in aqueous environments due to Vander Waal forces coupled with intrinsic agglomeration potential, are reported to influence the chemical stability of the nZVI impregnated TiO_2 nanocomposite material. The vibrational nodes for the metal-oxygen bonds Ti-O-Ti and Fe-O were identified in the 484–500 cm^{-1} range, which are critical for the structural support of nZVI by TiO_2 (Namakka et al., 2024). The Fe-O weak vibrational band at 500–742 cm^{-1} range, O-H bending at 1630 cm^{-1}, and O-H stretching nodes related to Fe-OH and Ti-OH species at 1600–1650, and 3400 cm^{-1} are associated to the adsorption of -OH functional group on the TiO_2 and nZVI respectively (Qureashi et al. 2024b). The consistent peaks profiles in this comparative spectral analysis confirmed a stable composite structure.

3.2 FESEM Analysis of TiO_2-nZVI Nanocomposite

The results of the FESEM images for the synthesized TiO_2-nZVI nanocomposite at x20,000 and x50,000 magnifications are shown in Fig. 4 (a and b). The morphological structure of the nZVI impregnated TiO_2 nanoparticle under magnifications of x15,000, the TiO_2-nZVI nanoparticle material exhibits regularly spherical shaped particles of uniform distribution, this characteristic morphological property was also observed in (Huang et al. 2018) a morphological trait commonly associated with the presence of mesoporous nZVI-based composites (Zahid et al. 2025).

Figure 5 shows the elemental mapping and spectral compositions of the synthesized nanocomposite material. The EDS spectra revealed a balanced mass ratio of nZVI and combined titanium and oxygen atoms with relatively higher mass ratio of Fe^{o}. The mass percent of iron, 57w% and sum of mass percent of oxygen and titanium atoms, 43 w% confirmed the existence of the TiO_2, Fe^{o} and possible formation of oxidized shell of the nZVI material as a layer coating the nanocomposite material. the compositional distribution and relative abundance of nanoparticles components are determined by interfacial interactions at the particle matrix, redox reactions that facilitate nanoparticle formation, and the nucleation to growth kinetics. These fundamental mechanisms are themselves highly dependent on the reaction pH in addition to other reaction parameters as established in prior studies (Hu et al. 2022; Namakka et al. 2023; Namakka et al., 2024; Xie et al. 2022).

The findings from EDS supported the results of the FTIR analysis and corroborated the successful impregnation of nZVI in the TiO_2 matrix with the desired elemental composition.

3.3 XRD Analysis of nZVI and TiO_2-nZVI Nanocomposite

Figure 6 shows the results of the XRD analysis of the nZVI and TiO_2-nZVI nanocomposite. The XRD peaks in Fig. 6(a) tabulated in Table 2 corroborates the existence of titanium dioxide, TiO_2 and a metallic zero valent iron, Fe^{o}. Similar findings were reported in (El-shafei et al. 2018; Hou et al. 2022; Liu et al. 2021; Sun et al. 2006). The most prominent peak at 25.3° is indexed to the 101 of the anatase phase (JCPDS No. 21–1272) was also observed in the recent findings of (Alam et al. 2025). This confirmed the presence of the TiO_2 catalytic component which forms the core of the synthesized TiO_2-nZVI nanocomposite and reinforces its overall stability and chemical activity (Biao et al. 2025). In a recent study, X García-Contreras et al. (2025) reported TiO_2 peaks at 2θ values of 37.9° and 38.56° assigned to the (004) and (112) crystal planes of the anatase phase (García-Contreras et al. 2025), consequently, the peak at 37.8° indexed 004 plane, 48.0° indexed 200 plane and a distinct peak corresponding to the 105 plane at 53.9° confirmed the formation of anatase phase of the TiO_2 component in the synthesized TiO_2-nZVI nanoparticles.

A distinct peak of nZVI, magnetic and reductive component of the TiO_2-nZVI nanocomposite, was observed at 44.7°, indexed (110) JCPDS 06–0696 which is the fingerprint

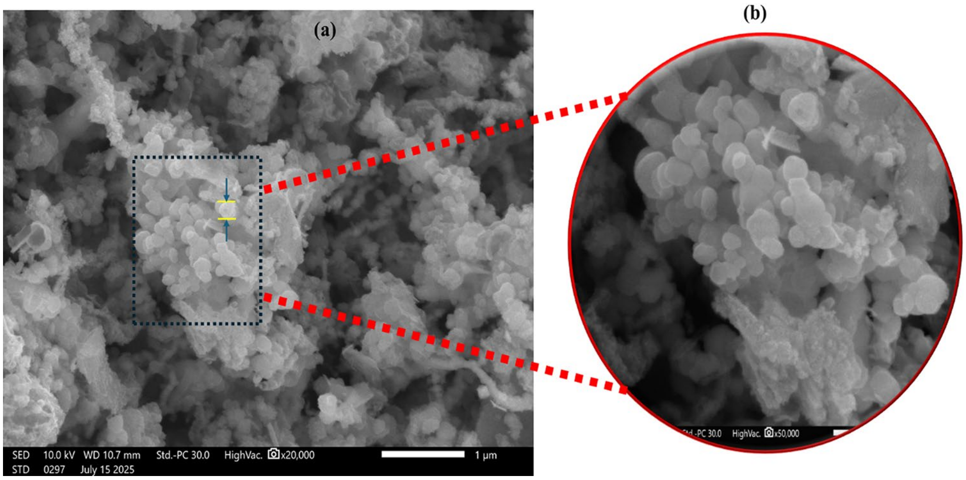

Fig. 4 FESEM analysis of synthesized TiO_2-nZVI nanoparticles **a** x20,000 magnification **b** selected area x50000 magnification

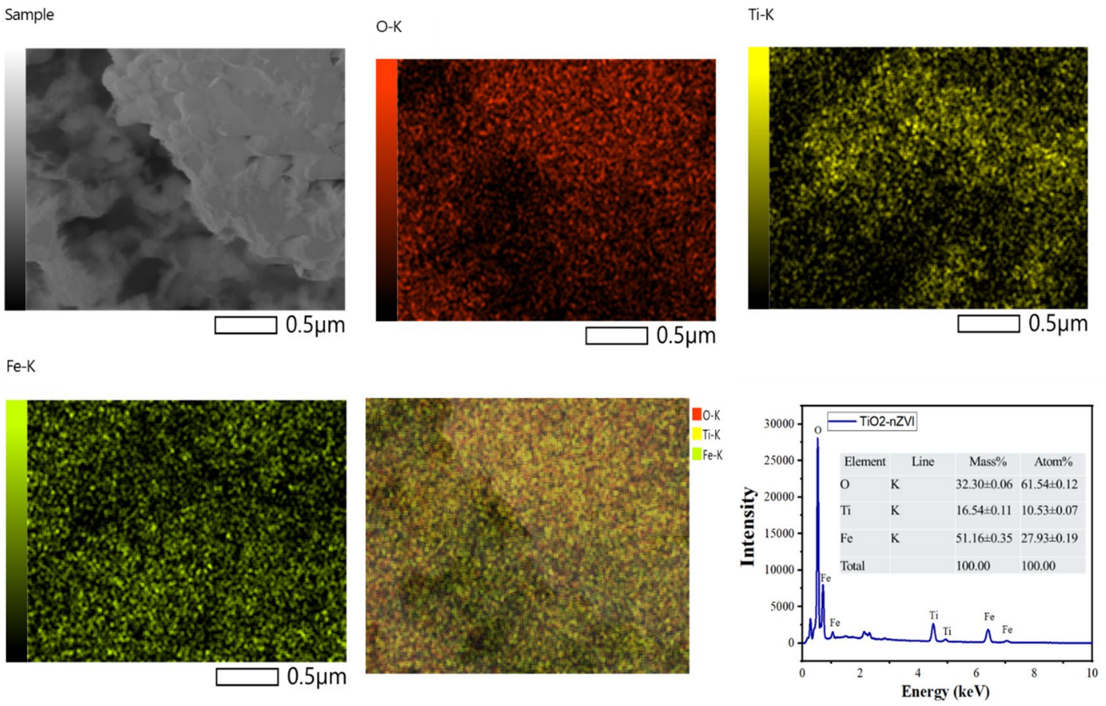

Element	Line	Mass%	Atom%
O	K	32.30±0.06	61.54±0.12
Ti	K	16.54±0.11	10.53±0.07
Fe	K	51.16±0.35	27.93±0.19
Total		100.00	100.00

Fig. 5 EDS analysis of the synthesized TiO_2-nZVI nanoparticles

Fig. 6 XRD pattern of nZVI and TiO_2-nZVI nanoparticles **a** TiO_2-nZVI **b** Comparison of diffraction patterns of ZVI and TiO_2-nZVI nanoparticles

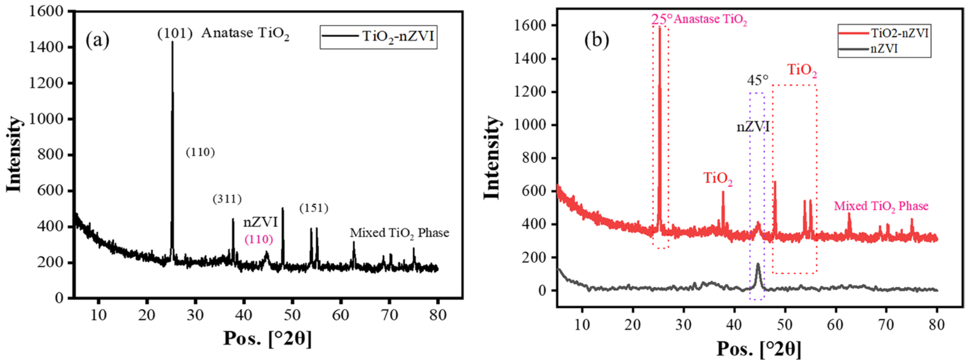

Table 2 XRD reflection index of the synthesized TiO_2-nZVI nanoparticles

Phase	2θ (°)	Crystal plane (hkl)	JCPDS Card	Ref.
TiO2 (Anatase)	25.3	(101)	21–1272	(Li et al. 2014)
TiO2 (Anatase)	37.8	(004)	21–1272	(Li et al. 2014)
TiO2 (Anatase)	48.0	(200)	21–1272	(Li et al. 2014)
TiO2 (Anatase)	53.9	(105)	21–1272	(Li et al. 2014)
Fe	44.7	(110)	06–0696	(Soria-Hernández et al. 2019)
Fe	65.1	(200)	06–0696	(Chen et al. 2019)

of the nZVI materials (Soria-Hernández et al. 2019). However, a small wide peak at 65.1° indexed to the iron (200) plane is associated with the Fe°. The peak reflection at 35.4° could be associated with the formation of iron oxide shells such as Fe_3O_4 and γ-Fe_2O_3 which form upon the exposure of Fe° to air during XRD analysis. However, these narrow passive layers usually produced via surface oxidation often serve to stabilize the highly reactive nZVI core (Ammar et al. 2020; Astuti et al., 2023; Yaghoobi et al. 2023).

3.4 XPS Analysis of TiO_2-nZVI Nanocomposite

Figure 7 illustrates the XPS analysis of the TiO_2-nZVI nanocomposite material. The full survey spectrum in Fig. 7(a) confirmed the presence of titanium (Ti), and iron (Fe), in the synthesized TiO_2-nZVI nanocomposite. Figure 7(b), deconvoluted via Gaussian model using origin software, provides a detailed survey of the chemical and electronic interaction of titanium spectrum Ti 2p showing a well-defined doublet of the Ti $2p_{3/2}$ and Ti $2p_{1/2}$ peaks observed at binding energy, BE = 458.7 eV and BE = 464.4 eV respectively.

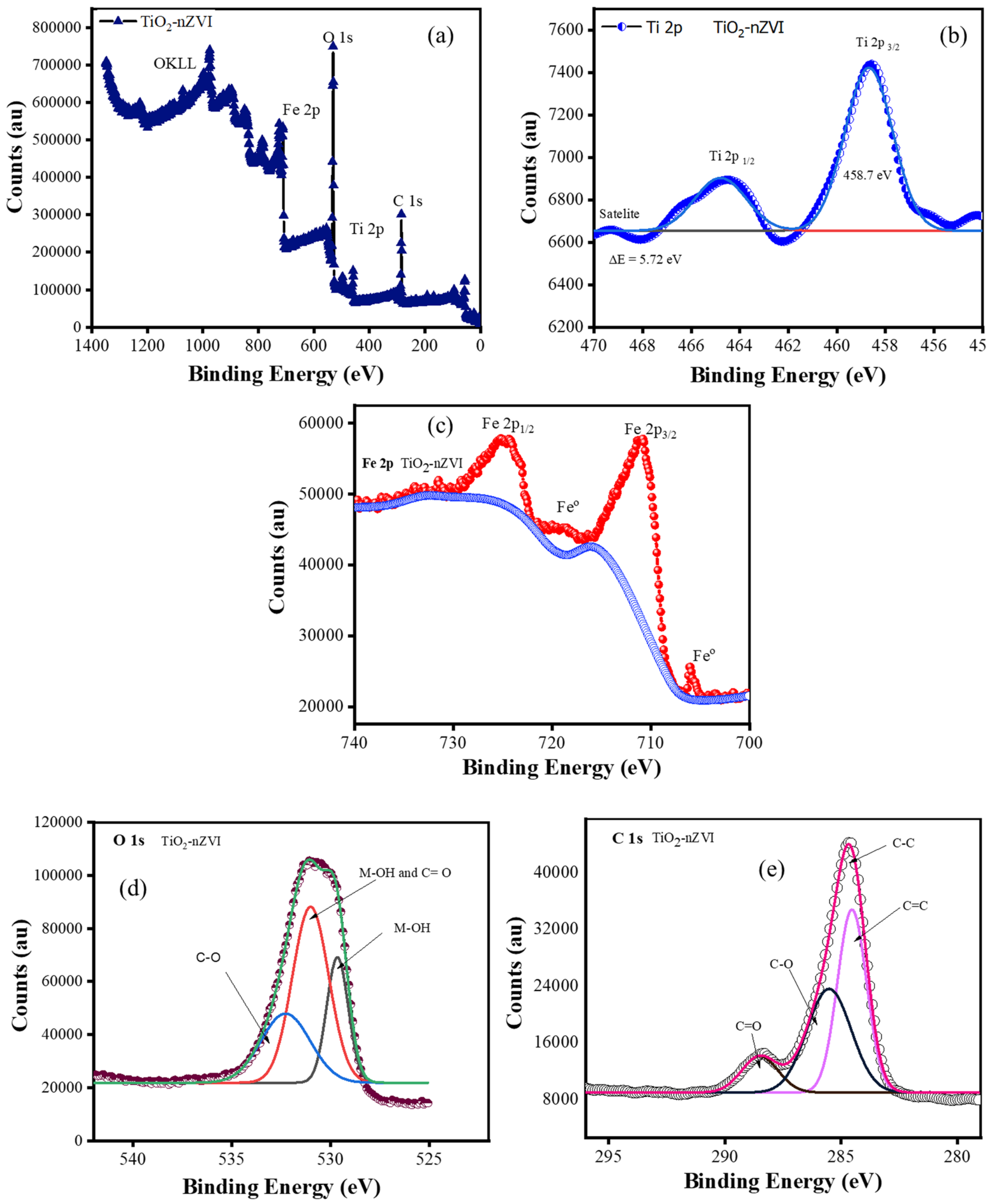

Fig. 7 TiO_2-nZVI XPS analysis. Full survey response (**a**), and (**b**-**e**) detailed survey of regions Ti 2p, Fe 2p, O 1 s, and C 1s

The peaks binding energy separation were found to be BE = 5.7 eV conforming with the predominant + 4 oxidation state, $Ti^{4+,}$ Similar findings were reported in(Chávez-Caiza et al. 2025) and (Kuspanov et al. 2024). The absence of Ti^{3+} suggest a successful integration of TiO_2 with the nZVI (Madan et al. 2020). The characteristic Fe $2p_{3/2}$ and Fe $2p_{1/2}$ spin orbit splitting peaks with two minor peaks located at BE = 705.6 eV and BE = 718.6 eV respectively are shown in Fig. 7c, which are consistent with the XPS findings in (Q. Li et al. 2021a, b, 2022). These minor peaks associated with lower intensities are characteristic property of nano Fe° (Wang et al. 2025). Subsequently, iron layers Fe $2p_{3/2}$ and Fe $2p_{½}$ located at BE = 711 eV and BE = 724.5 eV are a specific characteristic of oxidized Fe° passivated iron species Fe^{2+} and Fe^{3+} with a potential formation of Fe-OOH and Fe_3O_4 iron oxides (Ammar et al. 2020; Astuti et al., 2023), confirming the core shell structure of coated nZVI on TiO_2 nanoparticles. In the O 1 s spectrum (Fig. 7d), a prominent peak at approximately BE = 529 eV corresponds to the lattice oxygen bond in metal oxides (M-O), while a smaller deconvoluted peak at BE = 532.5 eV is attributed to O-H bonds (Jain et al. 2019; Tapia-P et al. 2021), confirming the presence of oxygen atoms associated with surface hydroxyl groups on TiO_2 and Fe-OOH or Fe_2O_3 (Botsa 2025). The detailed region analysis of the C 1 s XPS spectra was deconvoluted into four distinct peaks via similar Gaussian model (see Fig. 7e). The centered peak at BE = 284.8 eV is assigned to C-C and C-H bonds associated with adventitious hydrocarbon contaminants (Greczynski And Hultman 2017). The peak at BE = 286.0 eV to 287.0 eV and BE = 288.5 eV to 289.5 eV is attributed to oxidized C-O or C-OH and C = O or O-C = O functional groups (Bushell et al. 2019; Kwan et al. 2015). The presence of these oxidized byproducts could be associated with the exposure of adventitious carbon from residual organic precursors utilized in the nanoparticle synthesis to the atmospheric air. Recalling that the synthesized particles were washed several times with ethanol as described in Sec4.3.0. At low-binding energy BE = 283.0–284.0.0.0 eV signifies C-Metal bonds, particularly metal carbides such as Ti-C, Fe-C(Greczynski et al. 2018) and Ti-Fe-C (Wilhelmsson et al. 2010). However, there was no anatase peak indicating Ti-C bond which is commonly located near 281 eV, suggesting absence of carbon-oxygen replacement in the anatase TiO_2 lattice (Reghunath et al. 2021; Yu et al. 2020). The overall nanocomposite components selection was designed for synergistic activity, where the TiO_2 shell can facilitate the photocatalytic activity and enhanced electron transfer from the underlying nZVI, a mechanism known to boost contaminant reduction.

3.5 TGA Analysis of Individual nZVI Compared with TiO_2-nZVI Nanoparticles

Figure 8 shows the TGA of nZVI and compares the degradation properties with the nZVI impregnated TiO2 particles to evaluate the influence of the TiO_2 support on the thermal behavior and structural stability of the synthesized TiO_2-nZVI. From Fig. 8(a), the nZVI particles show multistage thermal degradation profile. The initial weight loss at the temperature range 51 °C to 120 °C is attributed to the evaporation of physically adsorbed moisture by the surface layer of the nZVI surface. While the continued weight loss observed at 284 °C, suggests the de-hydroxylation of surface iron oxyhydroxides that constitute the passivating shell of Fe^o. Similarly, the weight gain observed at 284 °C to 433 °C indicates the possible oxidation of the core Fe^o to FeO. In Fig. 8c, the initial degradation stage at 150 °C, characterized by 5 wt% to 8 wt% loss, is attributed to the removal of physiosorbed water and residual solvent molecules (Yu et al. 2019). Weight loss from 150 °C to 800 °C is associated with the decomposition of organic species, such as -O-H groups on the nanocomposite surface, and the previous stated oxidation of the nZVI core to iron oxides such as Fe_3O_4 or Fe_2O_3 (Koçak Soylu et al. 2025a) observed in Fig. 8a. The constant degradation of the composite material

Fig. 8 TGA Analysis of nZVI and TiO_2-nZVI (**a, c**), weight 1 st order differential of nZVI and TiO_2-nZVI (**b, d**) nanoparticles

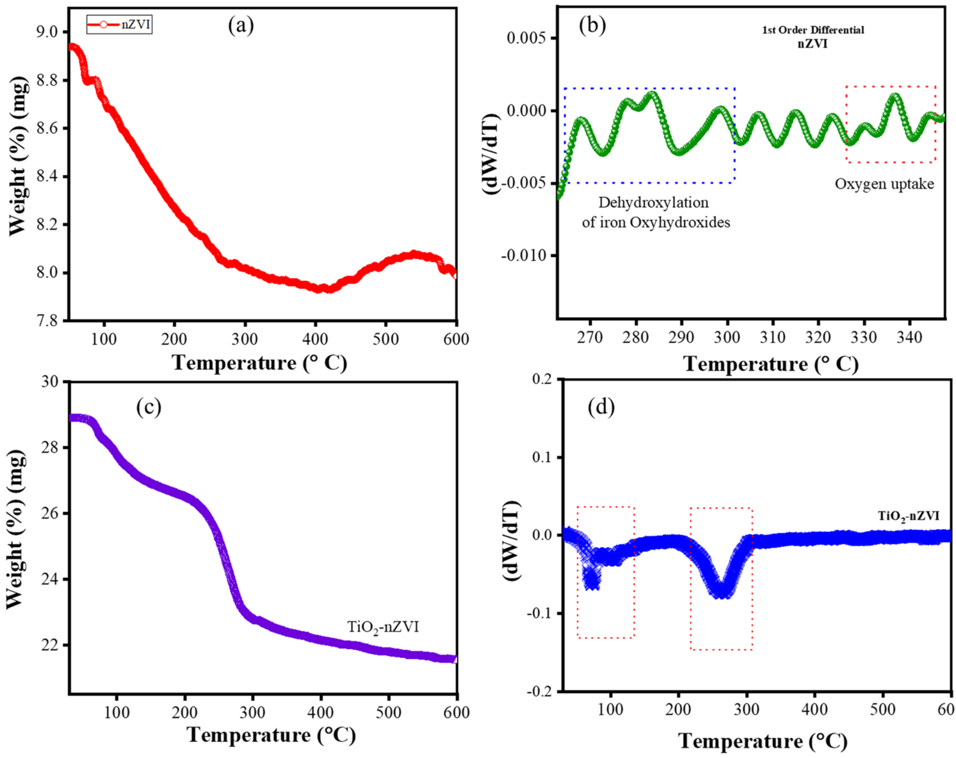

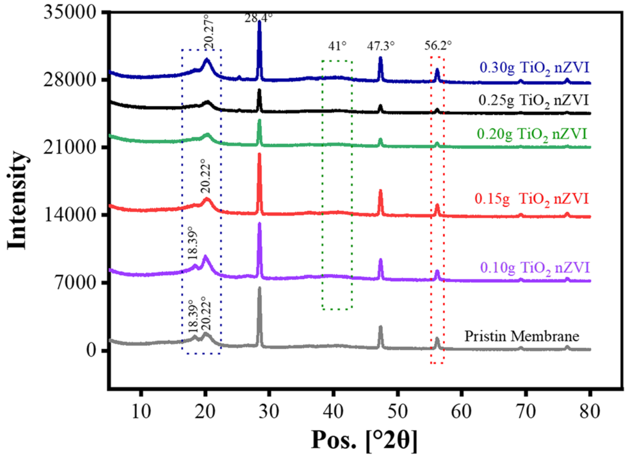

Fig. 9 XRD Analysis of pure PVDF and PVDF incorporated TiO_2-nZVI nanocomposite membranes at varying TiO_2-nZVI nanocomposite concentration (Ao = pristine PVDF; A1 = 0.1 g, A2 = 0.15 g, A3 = 0.20 g, A4 = 0.25 g and A5 = 0.3 g TiO_2-nZVI)

at this stage implies nearly complete oxidation of the reactive nZVI core and the initial exposure of TiO_2 shell.

3.6 Membrane Properties and Performance Evaluation

3.6.1 XRD Analysis

The XRD analysis results shown in Fig. 9 elucidate the crystalline structure and phase composition of the fabricated TiO_2-nZVI membranes modified with varying TiO_2-nZVI loadings, in comparison to the pristine membrane. From this figure, all the fabricated membranes show diffraction peaks at 2θ = ~18.39° associated to α-phase PVDF (Anand et al. 2020; Zaienah And Rezaur 2024; Zhang et al. 2020), and 2θ = 20.22° are characteristic of the electroactive β-phase of PVDF, a finding consistent with the previous findings in (Acarer-Arat et al. 2024; Ismail et al. 2021; James et al. 2024b, 2025; Zhang et al. 2023a, b). The diffraction observed at 2θ =~ 28.5° is indexed to the (101) TiO_2 crystal plane. The incorporation of nZVI is confirmed by the presence of peak at 2θ =~ 47.3° which changes with nanocomposite loadings, observed in the A1 to A5 compared to Ao, a distinct characteristic of Feo (110) plane. These behaviours are typical for nZVI in composite materials, often attributed to the small crystallite size of nZVI particles and the formation of an amorphous iron oxide shell Fe_3O_4 and FeOOH on the nanocomposite surface because of nZVI potential for rapid oxidation. This core-shell structure is a common feature in nZVI synthesis and is highly essential for nanocomposite stability and chemical reactivity. Additionally, the progressive variation in this peak's intensities observed with increasing TiO_2-nZVI loading provides a greater density of active sites on the nanocomposite membrane.

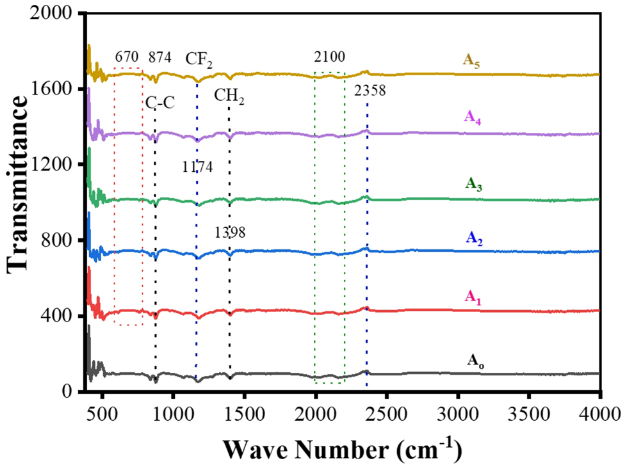

Fig. 10 FTIR Analysis of pristine PVDF and TiO_2-nZVI modified nanocomposite membranes (Ao = pristine PVDF; A1 = 0.1 g, A2 = 0.15 g, A3 = 0.20 g, A4 = 0.25 g and A5 = 0.30 g TiO_2- nZVI)

3.6.2 FTIR Analysis of the PVDF and Modified TiO_2-ZVI Nanocomposite Membranes

The results of the FTIR analysis of the PVDF- TiO_2-nZVI nanocomposite membranes shown in Fig. 7 confirmed the successful incorporation of TiO_2-nZVI nanocomposite in the membrane matrix and determined the interactions between the TiO_2-nZVI nanoparticles and PVDF membrane functional groups. The spectra of Ao, A1, A2, A3, A4, and A5 are moderately congruent, indicating that the incorporation of TiO_2-nZVI nanocomposite only slightly alters the fundamental chemical functionalities of the PVDF matrix particularly at lower wave numbers confirming the presence of additional functional groups in the membrane matrix. The peaks at 740 to 820 cm^{-1}, and 950 cm^{-1} and 960 cm^{-1} revealed consistent increase in hydrophilic Ti-O-H functional groups (Koçak Soylu et al. 2025b), confirming the incorporation of TiO_2 (Budiarti et al. 2017; Liu et al. 2024). The peak observed at 490 m^{-1} is attributed to 560 cm^{-1} Fe-O overlapping Ti-O stretching vibrations in the crystalline phases observed in the FTIR results of the nanocomposite material (refer to Fig. 1) (Fig. 10).

additional moderate deviation from **Ao** was observed on the modified membranes between 670 cm^{-1}, to 876 cm^{-1} C-C vibrations, potentially attributable to specific molecular rearrangement as TiO_2-nZVI were introduced in the PVDF membrane matrix, corroborating the XRD findings on the possible formation of metal carbide Ti-Fe-C (Wilhelmsson et al. 2010) and metal oxide such as Ti-O, Fe-O-, around 1250 cm^{-1} (Sun et al. 2018) where peaks broaden as TiO_2-nZVI nanocomposite loading increases.

3.6.3 Surface and Cross-Sectional Morphological Analysis of the PVDF - TiO_2-ZVI Nanocomposite Membranes

Figs. 11 and 12 show the results of the morphological characteristics of the PVDF-TiO_2-nZVI nanocomposite membranes utilizing FESEM-EDX analyses. The surface and cross-sectional morphologies, in Fig. 11; Table 3 reveal that incorporating the TiO_2-nZVI nanocomposite significantly influences the dispersion of nanoparticles within the PVDF matrix. At lower loadings of 0.1 g to 0.25 g, the TiO_2 and nZVI nanoparticles achieve a homogeneous distribution throughout the PVDF matrix. This optimal dispersion is critical for ensuring sustainable functional properties, enhancing membrane performance in applications such as filtration and separation processes. The interactions between the nanoparticles and the polymer matrix improve interfacial adhesion and enhance mechanical and permeability properties. In contrast, as the nanocomposite loading increases to 0.3 g, the particles agglomeration set in, this finding conformed with the previous studies that noted significant agglomeration issues at higher concentrations of TiO_2 (Gayatri et al. 2024) and nZVI (Li et al. 2021a, b; Ren et al. 2019) within nanocomposite membranes due to high surface energy. This agglomeration compromises the membrane's functional integrity by creating regions of high nanoparticle concentration, leading to decreased active surface area, hydrophilicity and effective utilization of membrane properties. The increased viscosity of the dope solution at higher loadings further limits nanoparticle mobility, resulting in clustering that undermines filtration performance (Fuzil et al. 2023; Kazemi et al. 2020b).

water flux analysis of PVDF

In addition to the concentration dependent morphological properties observed from FESEM analysis, results from the cross-sectional analysis corroborate the influence of nanocomposite loadings in the formation of extended macrovoids in the membrane structure (James et al. 2024a; Le et al. 2023; Rahman et al. 2024a, b). These morphological properties are associated to TiO_2-nZVI ability in enhancing the phase inversion process while promoting solvent to non-solvent exchange kinetics.it is imperative to mention that higher nanocomposite loading coupled with the increased particle agglomeration could compromise flux performance. Table 4 shows characteristics of fabricated nanocomposite membrane.

The porosity results shown in Table 3.0 are driven by thermodynamic parameters that influence the structural morphology and hydrophilic characteristics of the PVDF-TiO_2-nZVI nanocomposite membrane during the phase inversion. These parameters influence the stable interaction between the solvent and non-solvent interaction of the membrane at the various loading viz. 0.1 g to 0.15 g and 0.2 g to 0.3 g. The porosity 82.45%, 82.10%, and 86.58% for A1, A2 and A3 show uniform trend as particle loading increases with A4 (91.37%) recording highest porosity values. Although porosity alone does not determine hydrophilicity of the membrane matrix (Shokouhian And Solouki 2020; Silva et al. 2019). However, the trend provided an insight into the

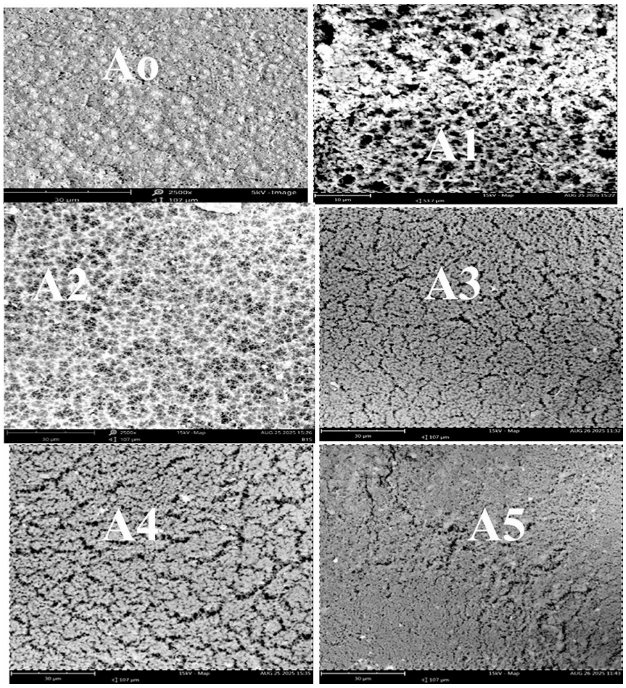

Fig. 11 Surface morphologies of the PVDF-TiO_2-nZVI nanocomposite membranes (Ao = pristine PVDF; A1 = 0.1 g, A2 = 0.15 g, A3 = 0.20 g, A4 = 0.25 g and A5 = 0.30 g TiO_2- nZVI). **b** Cross-sectional morphologies of the PVDF-TiO_2-nZVI nanocomposite membranes (Ao = pristine PVDF; A1 = 0.1 g, A2 = 0.15 g, A3 = 0.20 g, A4 = 0.25 g and A5 = 0.30 g TiO_2- nZVI)

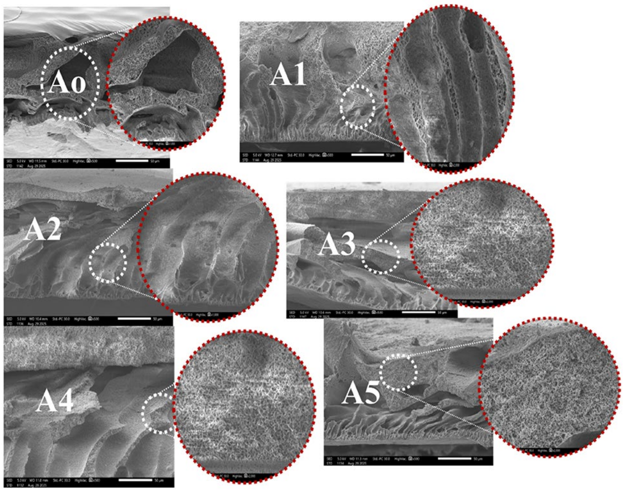

Fig. 12 Cross-sectional morphologies of the PVDF-TiO_2-nZVI nanocomposite membranes (Ao = pristine PVDF; A1 = 0.1 g, A2 = 0.15 g, A3 = 0.20 g, A4 = 0.25 g and A5 = 0.30 g TiO_2- nZVI)

morphological response of the nanocomposite membranes to particle loading. Consequently, hydrophilicity analysis was conducted to corroborate the hydrophilic behavior of the developed PVDF-TiO_2-nZVI.

Table 3 Characteristic properties of the PVDF TiO_2-$nZVI_2$ incorporated nanocomposite membranes

Modified membrane	Average membrane thickness (μm)	Membrane pore size $*10^{-3}$(μm)	Membrane porosity (%)
0.10 g TiO_2-nZVI	45.2	11.874	82.45
0.15 g TiO_2-nZVI	44.1	11.836	82.10
0.20 g TiO_2-nZVI	46.3	11.747	86.58
0.25 g TiO_2-nZVI	44.8	11.770	91.37
0.30 g TiO_2-nZVI	45.1	11. 746	89.33

3.6.4 Hydrophilicity, Solvent Content and Shrinkage Ratio Analysis of the Nanocomposite Membrane

Figs. 13 and 14 show the results of WCA analyses at various three locations on each of the developed PVDF-TiO_2-nZVI nanocomposite membranes, and the influence of drop age on the overall membrane WCA. The results indicate a significant decline in contact angles from the A0 to A5 with the pristine membranes. From this figure, the water contact

Table 4 Comparison of performance of PVDF-TiO_2-nZVI with other nanocomposites and nanocomposites modified membranes for contaminants remediation

Nanocomposite material	Contaminant(s)	Removal efficiency	Refs.
Melamine-modified UiO-66 (MUiO-66)	Pb^{2+} and Cd^{2+} under ambient conditions.	75%	(Abdelmoaty et al. 2022)
Gamma Irradiated Carboxymethyl Chitosan-Nanoclay Hydrogel ($CsAA_3Cl$)	Pb^{2+}, Ambient temperature.	84%	(El-Sayed Abdel-Raouf et al. 2023)
$NiMn_2O_4$@rGO nanocomposite	Hydroquinone	91%	(Subha et al. 2025)
$BaTiO_3$/NiO/g-C3N4 nanocomposite; MIL-88B(Fe)@CuS; Nitro-Modified NO2-MIL-53(Fe)	Tetracycline	78.2%	(Bai et al. 2025; Geng et al. 2025; Swarupa et al. 2025)
Cobalt nanoparticles (CoNPs) modified poly(methyl methacrylate-acrylic acid)-alginate [(Co-p(MAAG)] hydrogels	Rhodamine (Rh), under room temperature	96.35%	(Naseem et al. 2025)
Cu-complex@Fe3O4	4-methylbenzenethiol conversion	94%	(Razmara et al. 2025)
Cobalt based MOF	Antimicrobial remediation	74%	(Behl & Thakur, 2025)
Cobalt-based photocatalyst, Co-AAP-MOF; M0.2Ni0.8MoO_4; Bio Ag3PO4-ZnO; and MgAl LDH-Chitosan/Serpentine nanocomposite	MB dye and Congo dye, at ambient temperature	97%; 94.8%, 92.8%, and 35% respectively.	(Ali et al. 2025; Gamal et al. 2025; Hadkar And Selvaraj 2025; Younis et al. 2025)
Bi_2O_3/CuO and Fe-doped Bi_2O_3/CuO nanocomposite	Rhodamine B	85.17% and 93.1%	(Thamir et al. 2025; Zhang et al., 2025)
Gamma Irradiated Carboxymethyl Chitosan-Nanoclay Hydrogel ($CsAA_3Cl$)	Cr(VI) 100ppm, Ambient temperature.	93%	(El-Sayed Abdel-Raouf et al. 2023)
Polypropylene–Polypropylene-Grafted-Maleic Anhydride–Montmorillonite Clay Nanocomposite (PP-g-MA/MMT)	20ppm and 30ppm; 25 °C	55% and 15%	(Moja et al. 2018)
PVDF-PDA-TiO_2	Dye removal, 3 h treatment	88.8%	(Le et al. 2023)
PVDF-TiO_2@ZIF-67	10ppm Congo dye at ambient temperature; Neutral condition	84.84%	(Prabhakar et al. 2024)
PVDF-nZVI	2-chlorophenol (2-cp) wastewater	56% to 76%	(Li et al. 2021a, b)
PVDF-TiO_2-nZVI	10,20,30,40 and 40ppm	91% (optimal membrane), >80% across all concentrations	This study

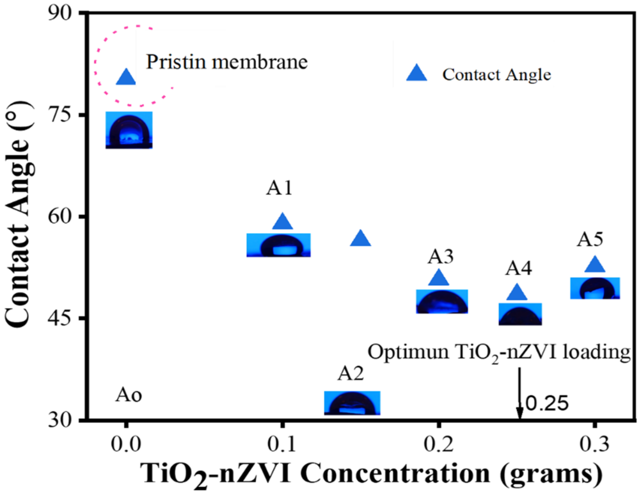

Fig. 13 Hydrophilicity assessment via membrane water contact angle analysis of PVDF - TiO$_2$-nZVI modified nanocomposite membranes with optical goniometer photographs (Ao = pristine PVDF; A1 = 0.1 g, A2 = 0.15 g, A3 = 0.20 g, A4 = 0.25 g and A5 = 0.3 g TiO$_2$-ZVI)

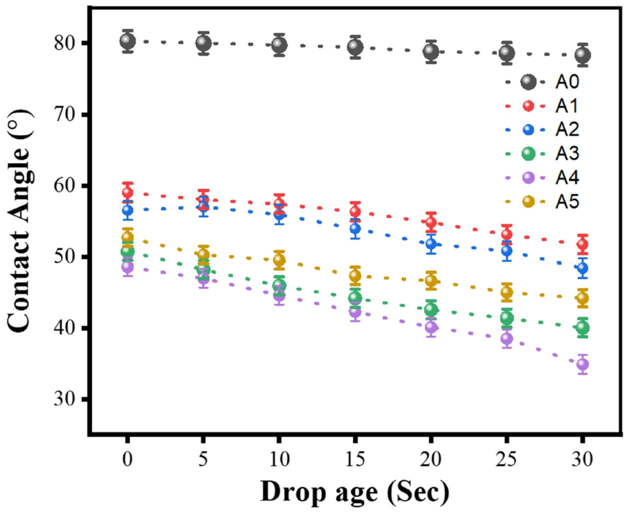

Fig. 14 Time dependent contact angle measurement analysis of PVDF- TiO$_2$-nZVI nanocomposite membranes (Ao = pristine PVDF; A1 = 0.1 g, A2 = 0.15 g, A3 = 0.20 g, A4 = 0.25 g and A5 = 0.3 g TiO$_2$-ZVI)

angle decrease from 80.29°, 58.99°, 56.51°, 50.74° and 48.58° for Ao to A4 followed by an upward value to 52.70 ° as the nanocomposite loading increased to 0.3 g, implying an increase in affinity to polar solvents with corresponding increase in nanocomposite loading which conforms with the results of XRD, SEM and the membrane characteristics highlighted in Table 3. The optimum value of 48.58° was attained at A4 nanocomposite concentration (see Fig. 13). This continuous decline in water contact angle corroborated an enhanced hydrophilic property of the hydrophobic PVDF surface due to modification of the membrane matrix by the synergistic effects of metallic nZVI (Silva et al. 2019) and incorporation of additional active sites of the hybrid TiO$_2$-nZVI nanoparticles. The increased surface wettability, which in turn reflects the hydrophilicity of the membrane surface is essential for enhanced membrane performance of membrane materials (Sun et al. 2013). The surface wettability is shown to increase with nanocomposite loading from A1 to A4 (0.1 g to 0.25 g TiO$_2$-nZVI) followed by an increase as the nanocomposite concentration reaches 0.30 g, this increase could be associated with particle aggregation as the dope solution viscosity increases with increase particle loadings. Consequently, the introduction of hydrophilic nanoparticles within the membrane matrix are reported to reduced contact angles, leading to improved water permeability and reduced fouling potential (Ahmed et al. 2024), corroborating the trend observed with increasing TiO$_2$-nZVI loading. Similar findings reported enhanced surface wetting properties associated with a decrease in membrane fouling, correlating improved hydrophilicity with superior membrane performance (Hurwitz et al. 2010b). The observed contact angles trend corroborates concentration dependent hydrophilicity properties of the developed membrane at moderate particles loading which conforms with findings by Hurwitz et al., (2010a) where membrane surface functionalization controls the surface energy of membranes resulting to a substantial decrease in contact angles, better wettability and operational efficiency.

However, water contact angle of the membrane materials varies significantly over time as the water drop ages, since the WCA is a time-dependent measurement (Zhao et al. 2023). Hence, Fig. 14 illustrates a time-dependent analysis of the water contact angle taken at 5-second intervals. The results indicate that the incorporation of TiO$_2$-nZVI in the membrane matrix considerably reduces the lifespan of the water drop on the membrane surface, as the water is absorbed by the membrane. This absorption leads to a decrease in both the water drop volume and the overall contact angle. These findings corroborate the initial membrane characteristics discussed in Tables 1 and 3 and the trends shown in Fig. 13, while giving insights into the flux performance of the nanocomposite membrane.

Figs. 15 and 16 show the results from solvent content analysis and the relationship between membrane porosity and solvent content (Fig. 16). The solvent content of the nanocomposite membrane was evaluated using water, methanol and ethanol with the relationship described in Eq. (8). From Fig. 15, water solvent contents increase with increase in nanocomposite membrane modification as the particle loading increased from A1 to A5 this align with the findings reported in (Nawaz et al. 2021). The water content progressively increases across the particle loading despite the decline in WCA observed at A5 in the previous section. Ao recorded the highest methanol and ethanol content

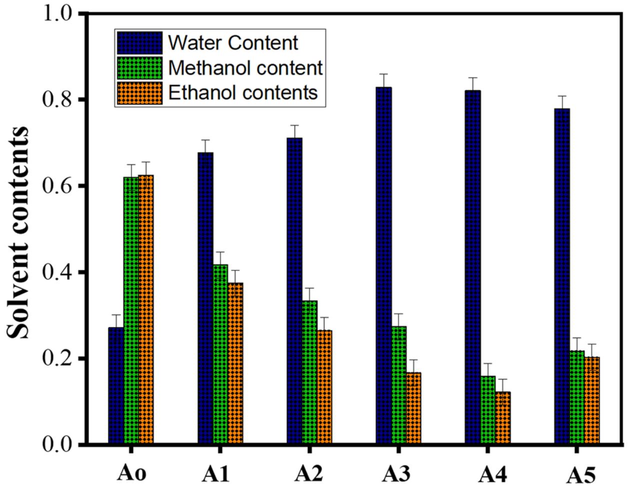

Fig. 15 Solvent content analysis using **a** Water, **b** methanol **c** Ethanol (Ao = pristine PVDF; A1 = 0.1 g, A2 = 0.15 g, A3 = 0.20 g, A4 = 0.25 g and A5 = 0.3 g TiO2-ZVI)

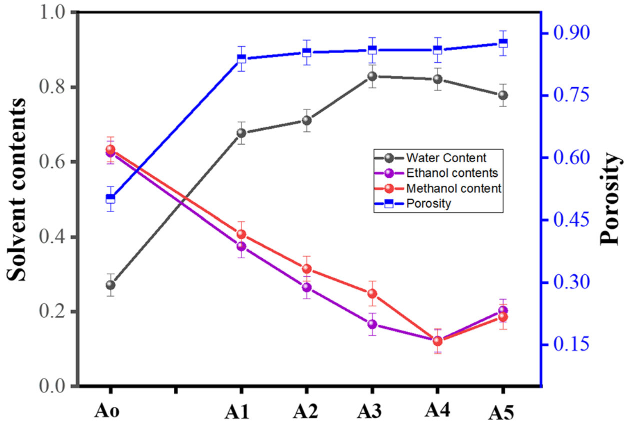

Fig. 16 Comparison of solvent content analysis using **a** Water, **b** methanol **c** Ethanol and membrane porosity (Ao = pristine PVDF; A1 = 0.1 g, A2 = 0.15 g, A3 = 0.20 g, A4 = 0.25 g and A5 = 0.3 g TiO_2-ZVI)

compared to water content; this increased methanol and ethanol content is associated with the increased WCA indicating hydrophobic properties of the unmodified membrane and its low affinity to water molecules. In Fig. 16 water, ethanol, and methanol contents are correlated to the porosity of the nanocomposite membrane. From this figure, as the water content increases, there is a corresponding uptick in membrane porosity, suggesting that higher water absorption corresponds to an enhanced structural permeability of the membrane material. This behaviour aligns with hydrophilic properties of polymer nanocomposite membranes, where water uptake facilitates membrane swelling (B et al. 2025). Conversely, the solvent content of ethanol and methanol increases with decreased porosity and membrane WCA.

3.6.5 Pure Water Flux and Heavy Metal Removal Analysis of the Nanocomposite Membrane

The results from the pure water flux analysis are shown in Fig. 17. The Pristine PVDF membrane attained steady flux values after 25 min of filtration which was quite faster in relation to the modified TiO_2-nZVI nanocomposite membrane which stabilizes at varying filtration time as the nanocomposite loading increases across the membrane material, with 40 min for 0.1 g (A1), 45 min for 0.15 g (A2) 50 min for 0.20 g and 0.25 g (A3 and A5) and about 65 min for 0.3 g (A4) nanocomposite membrane respectively. Despite these variations in steady flux filtration time, the steady water flux volume increases with increased nanocomposite loading from 27.95 L m^{-2} h^{-1}, 33.54 L m^{-2} h^{-1}, 17.143 L m^{-2} h^{-1}, 11.18 L m^{-2} h^{-1}, 10.43 L m^{-2} h^{-1}, to 6.020 L m^{-2} $h^{-1}$for the A5,A4, A3,A2,A1, and Ao respectively. The corresponding maximum pure water flux obtained for the corresponding membranes are 438.26 L m^{-2} h^{-1}, 573.91 L m^{-2} h^{-1}, 281.74 L m^{-2} h^{-1}, 203.48 L m^{-2} h^{-1}, 146.087 L m^{-2} h^{-1}, and 109.57 L m^{-2} h^{-1} for A5, A4, A3, A2, A1 and Ao respectively. The high flux performance observed in Fig. 17, which increases with higher nanocomposite loading, is associated with a decline in contact angle, indicating a significant enhancement in membrane hydrophilicity. These results align with previous hydrophilicity studies conducted by (Hurwitz et al. 2010a; Mun et al. 2018), solvent content analysis (Siddiqa et al. 2018) and the reported influence of hydrophilic properties on flux performance (Hao et al. 2025; Siddiqa et al. 2018). Other factors that could influence pure water flux performance apart from hydrophilicity are the membrane thickness, homogeneous interconnected pore network and agglomeration of membrane surface modification materials (Hamzah et al. 2019; Namakka et al. 2025; Sueraya et al. 2025). However, results from the morphological investigation, FESEM and membrane characteristics (see Table 3) corroborated consistent morphological structure and membrane thickness confirming the limited influence of these parameters on the observed overall flux performance of the nanocomposite membranes.

To determine the performance of the nanocomposite membrane material and identify the optimal nanocomposite loading, an initial concentration of 10 ppm lead (Pb^{2+}) solution was employed. The results from the filtration experiments with the modified nanocomposite membranes are illustrated in Figs. 18 and 19. A steady state removal rate for 10ppm Pb^{2+} was subsequently achieved, confirming the long-term stability of the nanocomposite membranes. The removal efficiencies shown in Fig. 18 were found to correlate with the increase in TiO_2-nZVI nanocomposite loading, with the optimal membrane configuration (A4) achieving a removal efficiency of 91% during the 50-minute

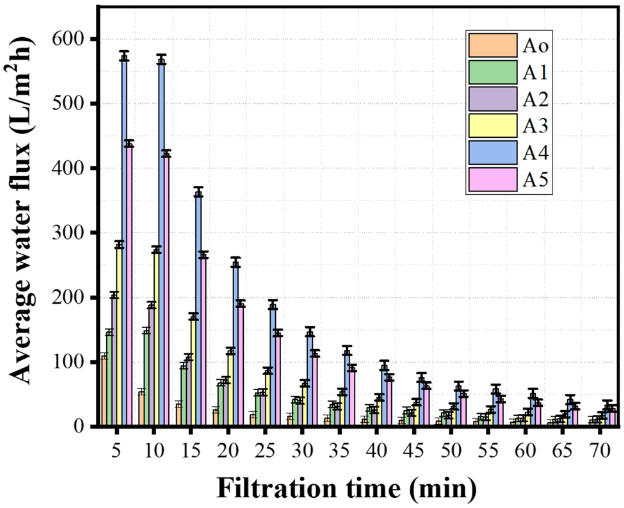

Fig. 17 Pure water flux analysis of PVDF-TiO₂-nZVI modified nanocomposite membranes (Ao = pristine PVDF; A1 = 0.1 g, A2 = 0.15 g, A3 = 0.20nanocomposite membranes at 10ppm g, A4 = 0.25 g and A5 = 0.3 g TiO_2-nZVI)

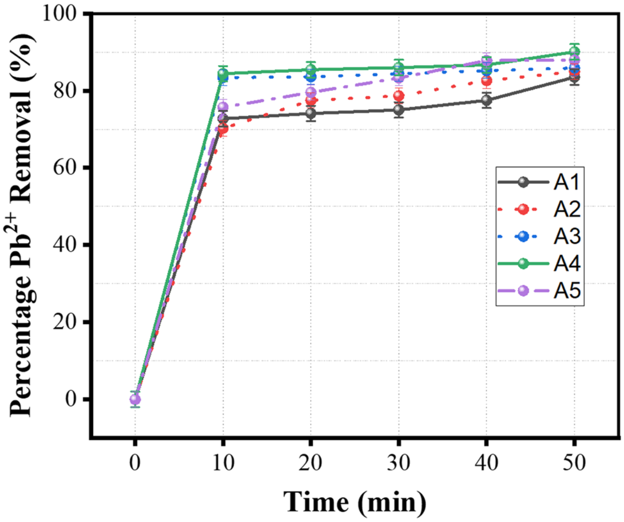

Fig. 18 Lead (Pb^{2+}) removal (%) analysis of PVDF-TiO₂-nZVI nanocomposite membranes at 10ppm concentration (Ao = pristine PVDF; A1 = 0.1 g, A2 = 0.15 g, A3 = 0.20 g, A4 = 0.25 g and A5 = 0.30 g TiO_2-nZVI)

filtration operation. This performance can be attributed to an increased number of reactive sites resulting from higher nanocomposite loading, as a greater proportion of nZVI and TiO_2 nanoparticles are incorporated into the membrane matrix, enhancing the synergistic capabilities for Pb^{2+} reduction and adsorption on the modified membrane surface. Similar findings were reported involving chromium (VI) (Kazemi et al. 2020b) removal using nZVI-TiO_2 nanocomposite membranes. The enhanced adsorption and reduction capabilities of the developed nZVI-TiO_2 components facilitate the production of reduced lead Pb^{2+} species which are subsequently retained by the modified membrane matrix. In Fig. 19, the concentration gradient exhibits a sharp decline across all membranes, followed by a plateau. This initial rapid decrease indicates the combined effects of surface adsorption and size exclusion, alongside oxidative-reductive reactions during the filtration process (Xiao et al. 2014). It is imperative to note that the mechanism involved in contaminants removal depends on the nature of the contaminants in addition to the catalytic activity of the nanocomposite membrane. For example, the disparity in the removal efficiencies observed in Pb^{2+} can be strongly influenced by the reaction mechanism involved. Since Pb^{2+} cations are easily reduced via chemical reduction into metallic lead or converted to Pb $(OH)_2$ or oxyhydroxide, which can be easily retained by the nanocomposite membrane matrix.

Figure 19 shows the results of the optimum membrane subjected to varying concentration of Pb^{2+} to investigate the influence of concentration on the removal efficiency of the membrane material under 20 ppm, 30 ppm, and 40 ppm concentrations. The results show progressive removal efficiency for all Pb^{2+} concentrations as over the filtration periods (10, 20 30 40 and 50 min). The overall optimum PVDF-TiO_2-nZVI nanocomposite membrane efficiencies are 88.5% ppm, 86.0%, 83.5% for 20ppm,30ppm and 40ppm respectively. This demonstrates a sustainable removal capacity and long-term membrane stability of the PVDF-TiO_2-nZVI for lead removal (Hadian et al. 2024). However, it equally highlighted a very critical concentration-dependent mechanism of the fabricated nanocomposite membrane observed in the initial stages of filtration operations. At the 30 min of the filtration treatment, the removal rates were 81% (20 ppm), 79% (30 ppm), and 78.3.0% (40 ppm) which was followed by an initial decrease in efficiency with decreasing concentration suggesting transitions from a reaction-site (adsorption) to a mass transfer (size exclusion) regime. This mechanism enabled higher concentration gradients at 30 ppm and 40 ppm to accelerate the mass transfer of Pb^{2+} ions towards the membrane surface, enhancing the removal efficiencies despite the limited reactive sites from the PVDF-TiO_2-nZVI surface. Although even below the 30 min of the filtration treatments the nano functional fillers (TiO2-nZVI particles) provided effective high density of reactive sites, however the initial influx of Pb^{2+} ions at 40 ppm certainly exceeded the instantaneous reaction rate, leading to the lowest initial removal efficiencies (Iron et al. 2023). The relatively excellent performance of the optimum membrane can be associated with balanced nanocomposite loading and coupled with the PVDF-TiO_2-nZVI dual-mechanism functionality, overcoming initial kinetic limitations over the treatment period. The possible removal mechanisms involve initial adsorption and simultaneous conversion of Pb^{2+} into insoluble, less mobile ion precipitates on

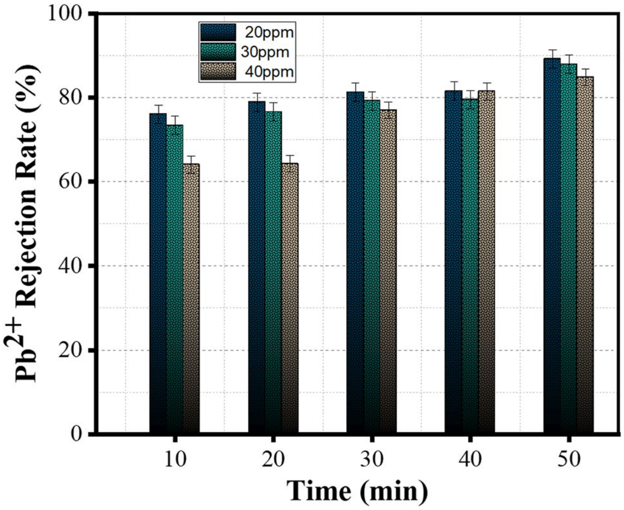

Fig. 19 Influence of concentration viz. 20pm,30ppm, and 40ppm on Pb^{2+} rejection rate of the optimal membrane (A4) over the 50 min filtration time

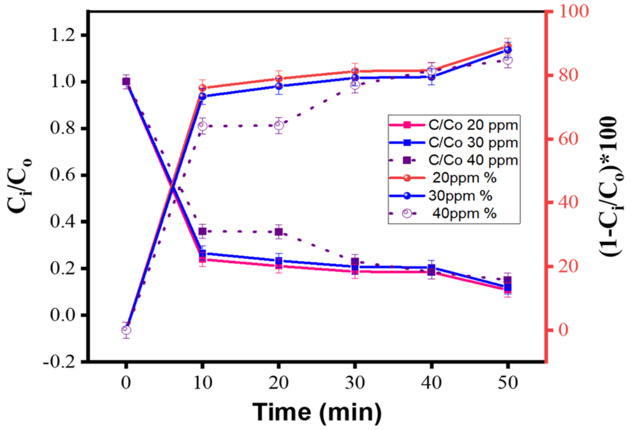

Fig. 20 Concentration gradient and Pb^{2+} removal efficiencies analysis of A4 PVDF-TiO_2-nZVI nanocomposite membranes at 20pm,30ppm, and 40ppm concentrations

the membrane surface, which maintains membrane flux and active site availability.

Figure 20 compared the results from the performance analysis of the PVDF-nZVI-TiO_2 nanocomposite under various concentration of Pb^{2+} with concentration gradient. the concentration gradient demonstrates that an increases in initial Pb^{2+} concentration correlates with lower percentage removal efficiencies due to increased competition between Pb^{2+} ions for reactive sites on the nanocomposite membrane surface thereby decreasing removal efficiencies. The removal efficiencies decreased with increasing Pb^{2+} concentration from 87% at 20ppm to 83% at 40ppm under the same filtration conditions. This is consistent with the recent findings on the removal efficiencies of heavy metals via adsorption mechanism (Ávila et al. 2025). The observed tend of the concentration gradients across the PVDF-TiO_2-nZVI nanocomposite membranes, particularly the steep declines at lower concentrations suggest the initial dominance of surface adsorption in the filtration mechanism. However, it imperative to note that both ion exclusion and surface adsorption mechanisms are crucial for an effective nanofiltration or reverse osmosis filtration operations (García-Ávila et al., 2025). As the concentration of Pb^{2+} ions increase from 20 ppm to 40 ppm, the saturation of reactive sites may lead to a plateau in Pb^{2+} removal efficiencies, indicative of the optimum adsorption capacity as more metal ions occupied the surface-active sites of the nanocomposite materials in the membrane matrix. Furthermore, the percentage removal efficiencies at 20 ppm and 30 ppm are significantly higher than at 40 ppm, reinforcing the negative impact of increase in initial concentration on membrane removal rate. This trend could be attributed to the suboptimal contact time between Pb^{2+} ions and the reactive sites within the membrane matrix, thereby restraining the heavy metal adsorption process. The consistent performance at lower concentrations signifies that the modified nanocomposite membranes are particularly effective under controlled conditions compared to other reported studies (See Table 4), as they utilize favorable adsorption dynamics and minimize the kinetic barriers that arise with significant metal ion competition in the membrane matrix.

3.6.6 PVDF-TiO_2-nZVI Long-Term Stability Studies

The long-term operational stability and potential leaching of oxidized iron of the optimal PVDF-TiO_2-nZVI nanocomposite membrane were evaluated following seven consecutive filtration cycles using a 5 ppm Pb^{2+} solution (see Figs. 21 and 22). From Fig. 21a gradual flux decline occurred following the first 50 min of filtration cycle, this flux decline becomes more pronounced after the second cycle (3 h of operation). The decline in hydraulic performance is associated with the deposition of surface foulants (Ezaier et al. 2024; Kirschner et al. 2019). However, the process was reversible, as hydraulic cleaning after 200 min effectively restored the membrane flux. Throughout the cycles, separation efficiency consistently exceeded 80% (refer to Fig. 22). These removal efficiencies demonstrate the robust structural integrity and stability of the optimal PVDF-TiO_2-nZVI nanocomposite membrane. These findings indicate sustained hydraulic stability and antifouling performance, which can be attributed to the membrane's enhanced hydrophilicity. Hydrophilic properties mitigate intermittent flux decline and reduce the conventional trade-off between hydraulic performance and pollutants remediation efficiencies of the nanocomposite membranes. The AAS analysis of the feed and permeate solutions after the successive cycles revealed 0.238 mg/L and 0.109 mg/L of

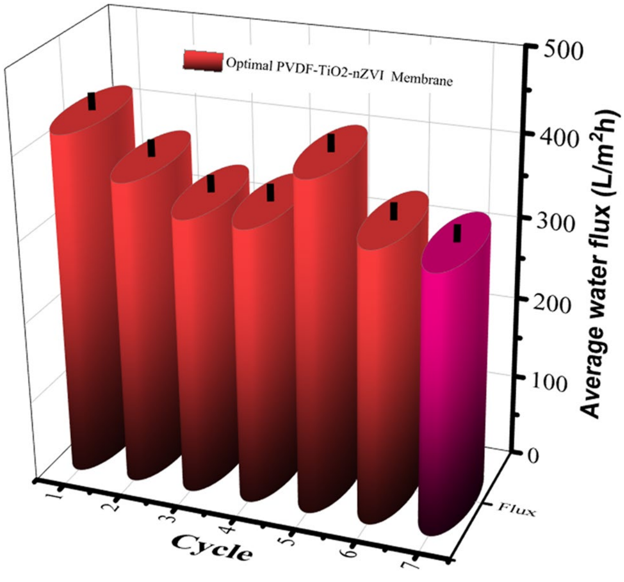

Fig. 21 Pure water flux analysis of optimal PVDF-TiO_2-nZVI modified nanocomposite membranes (A4 = 0.25 g TiO_2-ZVI) over 7 successive filtration cycles

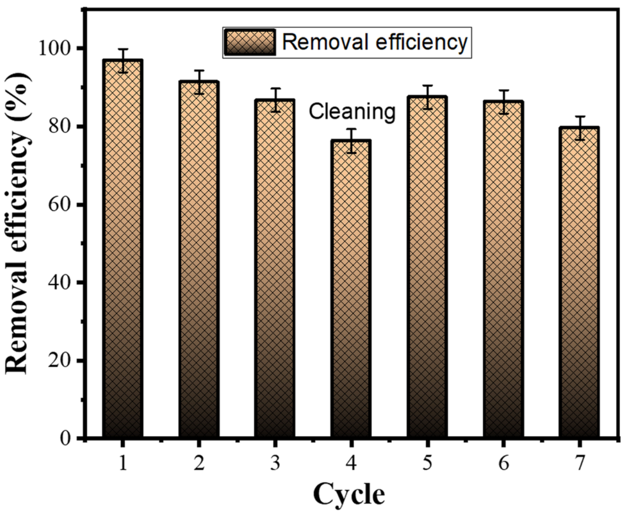

Fig. 22 Pb^{2+} removal analysis of the optimal PVDF-TiO_2-nZVI modified nanocomposite membrane (A4 = 0.25 g TiO_2-ZVI) over 7 successive filtration cycles at C_o = 5ppm

Fe ions respectively. This finding confirmed the leaching of oxidized Fe ions similar leaching of Fe composite potential were reported by (Minella et al. 2016). However, the Fe ions leached by the PVDF-TiO_2-nZVI are significantly within the acceptable range (≤0.3 mg/L) of iron in drinking water reported by world health organization in WHO/SDE/WSH/03.04/08 (World Health Organization 2003). This corroborates the potential utilization of the developed optimal membrane loading for a plethora of environmental applications.

The FTIR spectra comparing the optimal PVDF-TiO_2-nZVI nanocomposite membrane, A4 before and after Pb^{2+} treatment is shown in Fig. 23. The results of the FTIR after the 7 successive cycles revealed a shift in peak intensities at the corresponding functional group and provided evidence on the Pb^{2+} chemical interaction with the O-H functional groups within the PVDF-TiO_2-nZVI membrane matrix. Furthermore, there is an observed change in the shape and positions of Ti-O, Fe-O peaks at 1000–1200 cm^{-1}, these spectral changes corroborate the formation of a chemical bond or chelation complexes between the Pb^{2+} ions and the oxygen-containing functional groups of the PVDF-TiO_2-nZVI nanocomposite. The change in peaks intensities and shift of the -OH stretching vibrations peaks are highlighted in the range 2000–3500 cm^{-1} regions indicating active participation of these functional groups in binding Pb^{2+} ions contributing to the performance and long-term stability of the PVDF-TiO_2-nZVI nanocomposite membrane.

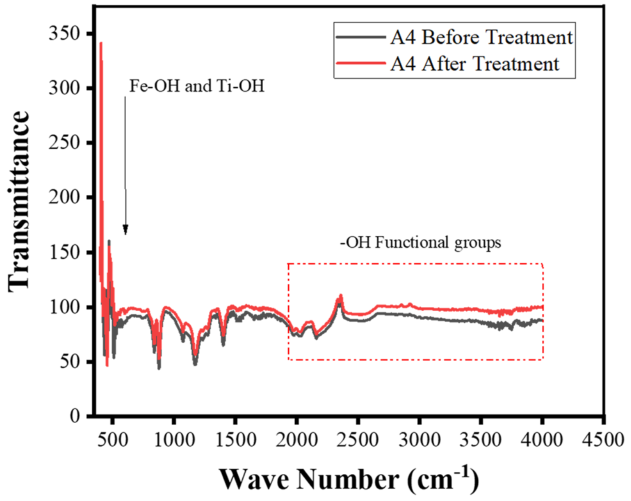

Fig. 23 FTIR Analysis of the optimal PVDF-TiO_2-nZVI nanocomposite membranes (A4 = 0.25gTiO_2- nZVI) before and after long term stability treatment

4 Conclusion

In conclusion, this study provided a comprehensive investigation of the synthesis, characterization, and performance evaluation of a novel PVDF-TiO_2-nZVI nanocomposite membrane for the removal of Pb^{2+} from aqueous solutions. The physicochemical properties of the synthesized TiO_2-nZVI nanocomposite were validated via various techniques with XPS and TGA analysis confirming the thermal stability and successful synthesis of TiO_2-nZVI nanocomposite. The developed PVDF-TiO_2-nZVI nanocomposite membrane showed stable hydraulic properties, enhanced hydrophilicity and long-term performance stability. The study identified an optimal loading of nanocomposite that maximizes membrane efficiency in removing lead ions from aqueous solutions. The optimum nanocomposite loading performance for the Pb^{2+} removal was found to be 91%. The removal efficiency exceeds 80% across all nanocomposite membranes and contaminants loadings. Hence, the incorporation of the TiO_2-nZVI nanocomposite into PVDF membranes significantly enhances their filtration performance and hydrophilicity, making them more effective for water treatment applications. However, further studies require the exploration of other parameters such as influence of pH on the membrane performance, effect of coexisting ions and potential chemical leaching of the nanocomposite materials from the membrane matrix.

Author Contributions Murtala Namakka conducted experiments and wrote the main manuscript text, Md Rezaur Rahman supervised and edited the manuscript, and Khairul Anwar Mohamed Bin Said supervised and secured research funding. All authors reviewed the manuscript.

Funding Open access funding provided by The Ministry of Higher Education Malaysia and Universiti Malaysia Sarawak. This work was funded by Universiti Malaysia Sarawak under the Vice Chancellor Higher Impact Research Scheme, Grant Number (UNI/FO2/VC-HIRG/85508/P10-03).

Data Availability No datasets were generated or analysed during the current study.

Declarations

Conflict of interests The authors declare no competing interests.

References

A. Anand, D. Meena, K.K. Dey, M.C. Bhatnagar, Enhanced piezoelectricity properties of reduced graphene oxide (RGO) loaded polyvinylidene fluoride (PVDF) nanocomposite films for nanogenerator application. J. Polym. Res. **27**(12), 1–11 (2020). https://doi.org/10.1007/S10965-020-02323-X/METRICS

A. Bushell, P. Mack, E. Grinstead, W. Sussex, (2019). Identifying structures on a plasma-modified polymer surface Authors. *Thermo Fisher Scientific Inc.*, *AN52333_E*, 3

A.C. Baily, T. Nunney, T.F. Scientific, E. Grinstead, W. Sussex, (n.d.). *XPS Analysis of a Hard Disk Platter by Rapid Depth Profiling APPLICATION NOTE*

A. James, M. Rezaur Rahman, K. Anwar Mohamed Said, M. Namakka, K. Kuok, M. Uddin Khandaker, J.Y. Al-Humaidi, R.H. Althomali, M.M. Rahman, Lithium chloride-mediated enhancement of dye removal capacity in Borneo bamboo derived nanocellulose-based nanocomposite membranes (NCMs). J. Mol. Liq. **413**(April), 125973 (2024b). https://doi.org/10.1016/j.molliq.2024.125973

A. James, M. Rezaur Rahman, K. Anwar Mohamed Said, M. Namakka, K. Kuok, M. Uddin Khandaker, J.Y. Al-Humaidi, R.H. Althomali, M.M. Rahman, Lithium chloride-mediated enhancement of dye removal capacity in Borneo bamboo derived nanocellulose-based nanocomposite membranes (NCMs). J. Mol. Liq. **413**(September), 125973 (2024a). https://doi.org/10.1016/j.molliq.2024.125973

A. James, M.R. Rahman, KAbin Mohamad Said, M. Namakka, M. Shahabuddin, M.S.M. Al-Saleem, J.Y. Al-Humaidi, M.M. Rahman, M.A. Salam, Multifunctional PVDF membranes incorporating graphene, TiO2, and nanocellulose: synergistic effects on filtration and antifouling performance. RSC Adv. **15**(38), 31471–31497 (2025). https://doi.org/10.1039/d5ra04672f

A.M. Khan, F. Russo, F. Macedonio, A. Criscuoli, E. Curcio, A. Figoli, The state of the art on PVDF membrane preparation for membrane distillation and membrane crystallization: towards the use of non-toxic solvents. Membranes **15**(4), 1–26 (2025). https://doi.org/10.3390/membranes15040117

A.M. Shaker, M. Khedawy, A.A. Moneer, N.M. El-Mallah, M.S. Ramadan, Loading of anionic surfactant on eco-friendly Biochar and its applications in Cr(VI) removal: adsorption, kinetics, and reusability studies. BMC Chem. **19**(1) (2025). https://doi.org/10.1186/s13065-024-01363-4

A.M. Younis, M. Tarek, T.H. Rakha, G.M.I.A. El-Reash, Synthesis and assessment of novel Co-AAP-MOF as a highly effective and reusable photocatalyst for the degradation of organic pollutants. J. Inorg. Organomet. Polym. Mater. **35**(10), 8552–8566 (2025). https://doi.org/10.1007/s10904-025-03797-2

A.M. Zafar, A. Naeem, M.A. Minhas, M.J. Hasan, S. Rafique, A. Ikhlaq, Removal of reactive dyes from textile industrial effluent using electrocoagulation in different parametric conditions of aluminum electrodes. Total Environ. Adv. **9**, 200087 (2024). https://doi.org/10.1016/j.teadva.2023.200087

A.Q. Jasim, S.K. Ajjam, Removal of heavy metal ions from wastewater using ion exchange resin in a batch process with kinetic isotherm. S. Afr. J. Chem. Eng. **49**, 43–54 (2024). https://doi.org/10.1016/j.sajce.2024.04.002

A. Qureashi, I. Nazir, K. Fatima, Zul Haq, F. Ahmad Ganaie, M. Rafiq, R. Saleem Khan, A. Hamid Rather, A. Bashir, A. Hussain Pandith, S. Majeed, F.A. Sheikh, Magnetic TiO2-nZVI nanofibers: a highly efficient platform for electrochemical dopamine detection. Mater. Sci. Eng. B Solid-State Mater. Adv. Technol. **310**, 117719 (2024a). https://doi.org/10.1016/J.MSEB.2024.117719

A. Qureashi, I. Nazir, K. Fatima, Zul Haq, F. Ahmad Ganaie, M. Rafiq, R. Saleem Khan, A. Hamid Rather, A. Bashir, A. Hussain Pandith, S. Majeed, F.A. Sheikh, Magnetic TiO2-nZVI nanofibers: a highly efficient platform for electrochemical dopamine detection. Mater. Sci. Eng. B Solid-State Mater. Adv. Technol. **310**, 117719 (2024b). https://doi.org/10.1016/j.mseb.2024.117719

A.S. Abdelmoaty, S.T. El-Wakeel, N. Fathy, A.A. Hanna, High performance of UiO-66 metal–organic framework modified with melamine for uptaking of lead and cadmium from aqueous solutions. J. Inorg. Organomet. Polym. Mater. **32**(7), 2557–2567 (2022). https://doi.org/10.1007/s10904-022-02326-9

A. Siddiqa, H. Razzaq, S. Qaisar, S. Liaqat, M. Arshad, R. Gill, (2018). *PVDF-Nanodiamonds Composite Membranes : Fabrication, Characterization and Water Treatment Applications CODEN*

(USA): PCHHAX PVDF-Nanodiamonds Composite Membranes : Fabrication, Characterization and Water Treatment Applications. *June*

A.Y. Kirschner, Y.H. Cheng, D.R. Paul, R.W. Field, B.D. Freeman, Fouling mechanisms in constant flux crossflow ultrafiltration. J. Membr. Sci. **574**, 65–75 (2019). https://doi.org/10.1016/j.memsci.2018.12.001

A. Zaienah, S. Rezaur, (2024). Impact of titanium dioxide / graphene in polyvinylidene fluoride nanocomposite membrane to intensify methylene blue dye removal, antifouling performance, and reusability. *April*, 1–14. https://doi.org/10.1002/app.56257

A.Z. Sueraya, M.R. Rahman, N.M. Sa'don, A. James, A. Bakri, M.K. Bin, M. Namakka, Polymer nanocomposite membranes for dye removal. Polym. Nanocomposite Membr. Water Treat. Desalin. 187–207 (2025). https://doi.org/10.1016/B978-0-443-23879-6.00006-3

B. Hao, W. Jarman, H. Peng, K. Li, A.M. Khan, F. Russo, F. Macedonio, A. Criscuoli, E. Curcio, A. Figoli, A. Siddiqa, H. Razzaq, S. Qaisar, S. Liaqat, M. Arshad, R. Gill, High performance crosslinked polyvinylidene fluoride (PVDF) membranes for solvent permeation. Membranes **209**, 106174 (2025). https://doi.org/10.3390/membranes15040117

B. He, W. Zhang, Y. Diao, S. Sun, Y. Zhang, W. Zhao, F. Wen, G. Yang, Mechanistic study of the adsorption capabilities of heavy metals on the surface of ferrihydrite: batch sorption, modeling, and density functional theory. RSC Adv. **15**(2), 1072–1080 (2025). https://doi.org/10.1039/d4ra07426b

B. Yan, Y. Dai, L. Xin, M. Li, H. Zhang, H. Long, X. Gao, Research progress in the degradation of printing and dyeing wastewater using chitosan based composite photocatalytic materials. Int. J. Biol. Macromol. **263**(2), 130082 (2024). https://doi.org/10.1016/j.ijbiomac.2024.130082

C.G. Soria-Hernández, L.M. Palacios-Pineda, A. Elías-Zúñiga, I.A. Perales-Martínez, O. Martínez-Romero, Investigation of the effect of carbonyl iron micro-particles on the mechanical and rheological properties of isotropic and anisotropic MREs: constitutive magneto-mechanical material model. Polymers (2019). https://doi.org/10.3390/polym11101705

C.K. Behl, A. Thakur, Investigating the functionality of a cobalt metal–organic framework for dye adsorption, antimicrobial and cytotoxicity activity. J. Inorg. Organomet. Polym. Mater. **35**(10), 8324–8349 (2025). https://doi.org/10.1007/s10904-025-03774-9

C.S. Ong, W.J. Lau, P.S. Goh, B.C. Ng, T. Matsuura, A.F. Ismail, Effect of PVP molecular weights on the properties of PVDF-TiO2 composite membrane for oily wastewater treatment process. Sep. Sci. Technol. (Philadelphia). **49**(15), 2303–2314 (2014). https://doi.org/10.1080/01496395.2014.928323

C. Zhang, D. Shi, C. Wang, G. Sun, H. Li, Y. Hu, X. Li, Y. Hou, R. Zheng, Pristine/magnesium-loaded biochar and ZVI affect rice grain arsenic speciation and cadmium accumulation through different pathways in an alkaline paddy soil. J. Environ. Sci. (China) **147**, 630–641 (2024). https://doi.org/10.1016/j.jes.2023.07.033

D. Fatta-Kassinos, M.I. Vasquez, K. Kümmerer, Transformation products of pharmaceuticals in surface waters and wastewater formed during photolysis and advanced oxidation processes - degradation, elucidation of byproducts and assessment of their biological potency. Chemosphere **85**(5), 693–709 (2011). https://doi.org/10.1016/j.chemosphere.2011.06.082

D.F.F. Brossault, T.M. McCoy, A.F. Routh, Self-assembly of TiO2/Fe3O4/SiO2 microbeads: a green approach to produce magnetic photocatalysts. J. Colloid Interface Sci. **584**, 779–788 (2021). https://doi.org/10.1016/j.jcis.2020.10.001

D. Gamal, A. Abd-Elkhalek, M. Shaban, S.I. Al-Saeedi, A.M. Elbasiony, G.H.A. El-Aziz, F. Mohamed, Insights into the structure and removal performance of cationic dyes by adsorption onto MgAl LDH-chitosan/serpentine nanocomposite. J. Inorg. Organomet. Polym. Mater. (2025). https://doi.org/10.1007/s10904-025-03917-y

D. Hadian, A. Alni, A. Patah, N. Handayani, M.A.L.I. Zulfikar, Efficient removal of Pb(II) ion using TiO2/ZnO/SiO2 nanocomposite from aqueous solutions via adsorption-photocatalysis process. Sains Malays. **53**(5), 1133–1147 (2024). https://doi.org/10.17576/jsm-2024-5305-13

D. Sharma, S. Kanchi, K. Bisetty, Biogenic synthesis of nanoparticles: a review. Arab. J. Chem. **12**(8), 3576–3600 (2019). https://doi.org/10.1016/j.arabjc.2015.11.002

D. Yu, Lead exposure in the 21st century: modeling a path from crisis to prevention. Eco-Environment & Health **4**(3), 100159 (2025). https://doi.org/10.1016/J.EEHL.2025.100159

E.C. Okpara, O.E. Fayemi, O.B. Wojuola, D.C. Onwudiwe, E.E. Ebenso, Electrochemical detection of selected heavy metals in water: a case study of African experiences. RSC Adv. **12**(40), 26319–26361 (2022). https://doi.org/10.1039/d2ra02733j

E.H. Khader, S.A. Muslim, N.M.C. Saady, N.S. Ali, I.K. Salih, T.J. Mohammed, T.M. Albayati, S. Zendehboudi, Recent advances in photocatalytic advanced oxidation processes for organic compound degradation: a review. Desalin. Water Treat. **318**, 100384 (2024). https://doi.org/10.1016/j.dwt.2024.100384

E. Sgreccia, C. Rogalska, F.S. Gallardo Gonzalez, P. Prosposito, L. Burratti, P. Knauth, M.L. Di Vona, Heavy metal decontamination by ion exchange polymers for water purification: counterintuitive cation removal by an anion exchange polymer. J. Mater. Sci. **59**(7), 2776–2787 (2024). https://doi.org/10.1007/s10853-024-09356-3

F. García-Ávila, A. Zambrano-Jaramillo, C. Velecela-Garay, K. Coronel-Sánchez, L. Valdiviezo-Gonzales, Effectiveness of membrane technologies in removing emerging contaminants from wastewater: reverse osmosis and nanofiltration. Water Cycle **6**, 357–373 (2025). https://doi.org/10.1016/j.watcyc.2024.12.004

F.G. Ávila, J. Cabrera-Sumba, S. Valdez-Pilataxi, J. Villalta-Chungata, L. Valdiviezo-Gonzales, C. Alegria-Arnedo, Removal of heavy metals in industrial wastewater using adsorption technology: efficiency and influencing factors. Cleaner Eng. Technol. (2025). https://doi.org/10.1016/j.clet.2025.100879

G.F. El-Said, H.A. Abdel-Mohsen, M.M. El-Sadaawy, M. Khedawy, A.H. Shobier, Ecotoxicological, ecological, and human health risks of total carbohydrates and some inorganic pollutants on the Nile Delta region along the Egyptian Mediterranean Coast. Mar. Pollut. Bull. **207**, 116816 (2024). https://doi.org/10.1016/j.marpolbul.2024.116816

G. Greczynski, D. Primetzhofer, L. Hultman, Reference binding energies of transition metal carbides by core-level x-ray photoelectron spectroscopy free from Ar+etching artefacts. Appl. Surf. Sci. **436**, 102–110 (2018). https://doi.org/10.1016/j.apsusc.2017.11.264

G. Greczynski, L. Hultman, C 1s peak of adventitious carbon aligns to the vacuum level: dire consequences for material's bonding assignment by photoelectron spectroscopy. ChemPhysChem **18**(12), 1507–1512 (2017). https://doi.org/10.1002/cphc.201700126

G.H. Major, V. Fernandez, N. Fairley, E.F. Smith, M.R. Linford, Guide to XPS data analysis: applying appropriate constraints to synthetic peaks in XPS peak fitting. J. Vacuum Sci. Technol. A **40**(6) (2022). https://doi.org/10.1116/6.0001975

G. Hurwitz, G.R. Guillen, E.M.V. Hoek, Probing polyamide membrane surface charge, zeta potential, wettability, and hydrophilicity with contact angle measurements. J. Membr. Sci. **349**(1–2), 349–357 (2010a). https://doi.org/10.1016/j.memsci.2009.11.063

G. Hurwitz, G.R. Guillen, E.M.V. Hoek, Probing polyamide membrane surface charge, zeta potential, wettability, and hydrophilicity with contact angle measurements. J. Membr. Sci. **349**(1–2), 349–357 (2010b). https://doi.org/10.1016/J.MEMSCI.2009.11.063

G. Swarupa, K.G. Rao, J. Ramchander, G. Upender, B.V. Kumar, Fabrication of ternary BaTiO3/NiO/g-C3N4 nanocomposite with superior charge separation for methyl orange and tetracycline degradation. J. Inorg. Organomet. Polym. Mater. (2025). https://doi.org/10.1007/s10904-025-03855-9

H.A. Budiarti, R.N. Puspitasari, A.M. Hatta, Sekartedjo, D.D. Risanti, Synthesis and characterization of TiO2@SiO2 and SiO2@TiO2 Core-Shell structure using Lapindo mud extract via Sol-Gel method. Procedia Eng. **170**, 65–71 (2017). https://doi.org/10.1016/j.proeng.2017.03.013

H. An, T. Liu, X. Xiao, M. Liu, Y. Hu, P. Wei, W. Yao, X. Tang, Y. Lai, X. Luo, S. Luo, Magnetic biochar-supported nanoscale zero-valent iron for remediation of arsenic and cadmium-contaminated soils: the role of free radicals. Environ. Res. (2025). https://doi.org/10.1016/j.envres.2025.121484

H. Hu, D. Zhao, C. Wu, R. Xie, Sulfidized nanoscale zerovalent iron supported by oyster powder for efficient removal of Cr (VI): characterization, performance, and mechanisms. Materials (2022). https://doi.org/10.3390/ma15113898

H. Nawaz, M. Umar, A. Ullah, H. Razzaq, K.M. Zia, X. Liu, Polyvinylidene fluoride nanocomposite super hydrophilic membrane integrated with Polyaniline-Graphene oxide nano fillers for treatment of textile effluents. J. Hazard. Mater. **403**, 123587 (2021). https://doi.org/10.1016/j.jhazmat.2020.123587

H. Zhang, Y. Zhu, L. Li, Fabrication of PVDF/graphene composites with enhanced β phase via conventional melt processing assisted by solid state shear milling technology. RSC Adv. **10**(6), 3391–3401 (2020). https://doi.org/10.1039/C9RA09459H

I.O. Ali, E.K. Alenezy, E.E. Salama, S. Alotibi, H. Nady, Sol-gel synthesis and enhanced catalytic performance of M0.2Ni0.8MoO4 (M = Cu2 + or Zn2+) for hydrogen evolution reaction and photocatalytic degradation of methylene blue dye. J. Inorg. Organomet. Polym. Mater. **4**, 9201–9220 (2025). https://doi.org/10.1007/s10904-024-03564-9

I.R. Chowdhury, S. Chowdhury, M.A.J. Mazumder, A. Al-Ahmed, Springer International Publishing, Removal of lead ions (Pb2+) from water and wastewater: a review on the low-cost adsorbents. Appl. Water Sci. (2022). https://doi.org/10.1007/s13201-022-01703-6

J. Chávez-Caiza, M. Navlani-García, J. Fernández-Catalá, A. Bhardwaj, C.M. Lousada, L.M. Belova, Berenguer-Murcia, D. Cazorla-Amorós, CuxO-modified inkjet printed TiO2 thin films photocatalysts for hydrogen production from water splitting. Catal. Today. **453**, 115273 (2025). https://doi.org/10.1016/J.CATTOD.2025.115273

J. Hou, Y. Li, H. Ci, L. Miao, G. You, J. Wu, Y. Xu, Influence of aggregation and sedimentation behavior of bare and modified zero-valent-iron nanoparticles on the Cr(VI) removal under various groundwater chemistry conditions. Chemosphere (2022). https://doi.org/10.1016/j.chemosphere.2022.133905

J. Mun, H.M. Park, E. Koh, Y.T. Lee, Enhancement of the crystallinity and surface hydrophilicity of a PVDF hollow fiber membrane on simultaneous stretching and coating method. J. Ind. Eng. Chem. **65**, 112–119 (2018). https://doi.org/10.1016/j.jiec.2018.04.019

J. Ren, Y.C. Woo, M. Yao, S. Lim, L.D. Tijing, H.K. Shon, Nanoscale zero-valent iron (nZVI) immobilization onto graphene oxide (GO)-incorporated electrospun polyvinylidene fluoride (PVDF) nanofiber membrane for groundwater remediation via gravity-driven membrane filtration. Sci. Total Environ. **688**, 787–796 (2019). https://doi.org/10.1016/J.SCITOTENV.2019.05.393

J.S. Schneider, Neurotoxicity and outcomes from developmental lead exposure: persistent or permanent? Environ. Health Perspect. **131**(8), 1–5 (2023). https://doi.org/10.1289/EHP12371

J. Sun, H. Bi, S. Su, H. Jia, X. Xie, L. Sun, One-step preparation of GO/SiO2 membrane for highly efficient separation of oil-in-water emulsion. J. Membr. Sci. **553**, 131–138 (2018). https://doi.org/10.1016/j.memsci.2018.02.029

J. Tapia-P, J. Gallego, J.F. Espinal, Calcination temperature effect in catalyst reactivity for the CO SELOX reaction using Perovskite-like LaBO3 (B: Mn, Fe, Co, Ni) oxides. Catal. Lett. **151**(12), 3690–3703 (2021). https://doi.org/10.1007/s10562-021-03601-z

K.H. Thamir, H.A. Ahmed, S.Z. Al-Ashoor, P. Kanjariya, M. Akku, R. Thakur, G.D.A. Jebaselvi, S. Choudhury, M.A. Rusho, H.M. Alkahtani, Hydrothermally synthesized Fe-doped bismuth oxide/CuO nanocomposites for efficient photocatalytic degradation of Rhodamine B. J. Inorg. Organomet. Polym. Mater. **35**(10), 8249–8267 (2025). https://doi.org/10.1007/s10904-025-03722-7

K.M. Abdelsalam, H.R.Z. Tadros, A.A. Moneer, M.K. Khalil, S.K. Hamdona, L. Shakweer, M.N. Moawad, A.A.M. El-Sayed, G.F. El-Said, M.M. Ismail, A.H. Shobier, S. Hosny, A.S. Dabbous, A.M. Alzeny, M. Khedawy, The Egyptian Nile estuarine habitats: a review. Aquat. Sci. **86**(4), 1–29 (2024). https://doi.org/10.1007/s00027-024-01111-9

K. Naseem, S. Haider, K. Alam, Cobalt nanoparticles loaded poly(methyl methacrylate) nanocomposite hydrogels for the catalytic reduction of Rhodamine B; a toxic dye. J. Inorg. Organomet. Polym. Mater. **35**(10), 8734–8748 (2025). https://doi.org/10.1007/s10904-025-03812-6

K. Xiao, J. Sun, Y. Mo, Z. Fang, P. Liang, X. Huang, J. Ma, B. Ma, Effect of membrane pore morphology on microfiltration organic fouling: PTFE/PVDF blend membranes compared with PVDF membranes. Desalination. **343**, 217–225 (2014). https://doi.org/10.1016/j.desal.2013.09.026

L.A. García-Contreras, J.O. Flores-Flores, R. Zanella, J.Á. Arenas-Alatorre, J.Á. Chávez-Carvayar, Photocatalytic performance of 1D-TiO2 with flower-like morphology and tunable anatase, brookite, and rutile phases for ibuprofen degradation. Ceram. Int. **51**(28), 56029–56049 (2025). https://doi.org/10.1016/J.CERAMINT.2025.09.317

L. Liu, J. Zhao, X. Liu, S. Bai, H. Lin, D. Wang, Reduction and removal of As(V) in aqueous solution by Biochar derived from nano zero-valent-iron (nZVI) and sewage sludge. Chemosphere. **277**, 130273 (2021). https://doi.org/10.1016/j.chemosphere.2021.130273

L.L.S. Silva, J.A. Caldara, A.M. Rocco, C.P. Borges, F.V. Fonseca, Evaluation of nano zero-valent iron (nZVI) activity in solution and immobilized in hydrophilic PVDF membrane for drimaren red X-6BN and bisphenol-a removal in water. Processes (2019). https://doi.org/10.3390/PR7120904

L. Wang, C. Song, X. Jiang, T. Li, H. Wang, Mechanochemical synthesis of redox-active Fe-based nanocomposites for efficient Cr(VI) remediation in water and soil. Sep. Purif. Technol. **377**(1), 134212 (2025). https://doi.org/10.1016/j.seppur.2025.134212

L. Zhang, Y. Zhu, H. Gu, S.S. Lam, X. Chen, C. Sonne, W. Peng, A review of phytoremediation of environmental lead (pb) contamination. Chemosphere **362**, 142691 (2024). https://doi.org/10.1016/j.chemosphere.2024.142691

M.A. Ahmed, S.A. Mahmoud, A.A. Mohamed, Nanomaterials-modified reverse osmosis membranes: a comprehensive review. RSC Adv. **14**(27), 18879–18906 (2024). https://doi.org/10.1039/d4ra01796j

M.A. Alam, S. Ahmed, R.K. Bishwas, S. Mostofa, S.A. Jahan, X-ray crystallographic diffraction study by whole powder pattern fitting (WPPF) method: refinement of crystalline nanostructure polymorphs TiO2. S. Afr. J. Chem. Eng. **51**, 68–77 (2025). https://doi.org/10.1016/J.SAJCE.2024.10.010

M.A. Tofighy, T. Mohammadi, M.H. Sadeghi, High-flux PVDF/PVP nanocomposite ultrafiltration membrane incorporated with graphene oxide nanoribbones with improved antifouling properties. J. Appl. Polym. Sci. **138**(4), 1–15 (2021). https://doi.org/10.1002/app.49718

M.C. Benalia, L. Youcef, M.G. Bouaziz, S. Achour, H. Menasra, Removal of heavy metals from industrial wastewater by chemical precipitation: mechanisms and sludge characterization. Arab. J. Sci. Eng. **47**(5), 5587–5599 (2022). https://doi.org/10.1007/s13369-021-05525-7

M. El-Sayed Abdel-Raouf, R.S. Kamal, D.E. Hegazy, A. Sayed, Gamma irradiation synthesis of carboxymethyl chitosan-nanoclay hydrogel for the removal of Cr(VI) and Pb(II) from aqueous media. J. Inorg. Organomet. Polym. Mater. **33**(4), 895–913 (2023). https://doi.org/10.1007/s10904-023-02543-w

M. Kazemi, M. Peyravi, M. Jahanshahi, Multilayer UF membrane assisted by photocatalytic NZVI@TiO2 nanoparticle for removal and reduction of hexavalent chromium. J. Water Process Eng. (2020a). https://doi.org/10.1016/j.jwpe.2020.101183

M. Kazemi, M. Peyravi, M. Jahanshahi, Multilayer UF membrane assisted by photocatalytic NZVI@TiO2 nanoparticle for removal and reduction of hexavalent chromium. J. Water Process Eng. **37**, 101183 (2020b). https://doi.org/10.1016/j.jwpe.2020.101183

M. Khedawy, A.A. Moneer, A.M. Shaker, M.S. Ramadan, E.A. Fadl, Marine algae-mediated PVDF/ZnO nanocomposite ultrafiltration membranes: superior performance in Cr(VI) removal from aqueous solutions. Environ. Sci. Pollut. Res. **32**(30), 17997–18013 (2025). https://doi.org/10.1007/s11356-025-36715-7

M.M. El-Sadaawy, G.F. El-Said, M. Khedawy, A.A. Moneer, Development of a cost-effective bipolar electrocoagulation system for enhanced hexavalent chromium removal: empirical modeling and statistical optimization. Discover Appl. Sci. **7**(12) (2025). https://doi.org/10.1007/s42452-025-07987-y

M.M. El-shafei, A. Hamdy, M.M. Hefny, (2018). *Zero-valent iron nanostructures: synthesis, characterization and application*. *January*

M. Minella, E. Sappa, K. Hanna, F. Barsotti, V. Maurino, C. Minero, D. Vione, Considerable fenton and photo-Fenton reactivity of passivated zero-valent iron. RSC Adv. **6**(89), 86752–86761 (2016). https://doi.org/10.1039/c6ra17515e

M. Namakka, M.R. Rahman, K.A. Bin Mohamad Said, A. Muhammad, Insights into micro-and nano-zero valent iron materials: synthesis methods and multifaceted applications. RSC Adv. **14**(41), 30411–30439 (2024). https://doi.org/10.1039/d4ra03507k

M. Namakka, M.R. Rahman, K.A. Mohamad Bin Said, K.K. Kuok, F.A. Md Yusof, M.S.M. Al-Saleem, J.Y. Al-Humaidi, M.M. Rahman, Unveiling the synergistic effect of an nZVI–SiO2–TiO2 nanocomposite for the remediation of dye contaminated wastewater. Mater. Adv. (2024a). https://doi.org/10.1039/D4MA00853G

M. Namakka, M.R. Rahman, K.A. Mohamad Bin Said, K.K. Kuok, F.A. Md Yusof, M.S.M. Al-Saleem, J.Y. Al-Humaidi, M.M. Rahman, Unveiling the synergistic effect of an nZVI–SiO 2 –TiO 2 nanocomposite for the remediation of dye contaminated wastewater. Mater. Adv. (2024b). https://doi.org/10.1039/D4MA00853G

M. Namakka, M.R. Rahman, K.A.M. Said, M. Abdul Mannan, A.M. Patwary, A review of nanoparticle synthesis methods, classifications, applications, and characterization. Environ. Nanotechnol. Monit. Manag. **20**(September), 100900 (2023). https://doi.org/10.1016/j.enmm.2023.100900

M. Namakka, M.R. Rahman, N.M. Sa'don, M.K. Bakri, Bin, A.Z. Sueraya, Chemisorption and physisorption of polymer nanocomposite membranes. Polym. Nanocomposite Membr. Water Treat. Desalin. 423–446 (2025). https://doi.org/10.1016/B978-0-443-23879-6.00011-7

M.R. Rahman, A. James, K.A. Mohamed Said, M. Namakka, M.U. Khandaker, W.H. Jiunn, J.Y. Al-Humaidi, R.H. Althomali, M.M. Rahman, A TiO 2 grafted bamboo derivative nanocellulose polyvinylidene fluoride (PVDF) nanocomposite membrane for wastewater treatment by a photocatalytic process. Mater. Adv. (2024). https://doi.org/10.1039/d4ma00716f

M.R. Rahman, A.Z. Sueraya, K.A.B.M. Said, M. Namakka, A. James, I.M.M. Rahman, M.S.M. Al-Saleem, J.Y. Al-Humaidi, M.M. Rahman, Impact of graphene/nanocellulose on nanocomposite membrane for methylene blue dye removal and antifouling performance. J. Appl. Polym. Sci. (2025a). https://doi.org/10.1002/app.57648

M.R. Rahman, A.Z. Sueraya, K.A.B.M. Said, M. Namakka, A. James, I.M.M. Rahman, M.S.M. Al-Saleem, J.Y. Al-Humaidi, M.M. Rahman, Impact of graphene/nanocellulose on nanocomposite membrane for methylene blue dye removal and antifouling performance. J. Appl. Polym. Sci. (2025b). https://doi.org/10.1002/app.57648

M. Shokouhian, S. Solouki, P-phenylenediamine-grafted multi-walled carbon nanotubes as a hydrophilic modifier in thin-film nanocomposite membrane. Polym. Bull. **77**(7), 3485–3498 (2020). https://doi.org/10.1007/s00289-019-02899-5

M. Yaghoobi, F. Asjadi, M. Sanikhani, A facile one-step green hydrothermal synthesis of paramagnetic Fe3O4 nanoparticles with highly efficient dye removal. J. Taiwan Inst. Chem. Eng. (2023). https://doi.org/10.1016/j.jtice.2023.104774

M. Zahid, Z.U.H. Khan, S. Sabahat, M.M.S. Abdullah, N.S. Shah, N. Muhammad, Photocatalytic degradation of norfloxacin using biochar supported nZVMn/TiO₂ nanocomposite: synthesis, characterization, and performance evaluation. Surf. Interfaces **72**, 107034 (2025). https://doi.org/10.1016/j.surfin.2025.107034

N. B, R. Ambedkar, G. Shanker, S. Singh, Investigation of photo-Fenton assisted antibiotic degradation using nZVI/Cu bimetallic heterostructures embedded PVDF film. Surf. Interfaces **72**, 107122 (2025). https://doi.org/10.1016/j.surfin.2025.107122

N. Hamzah, C.P. Leo, B.S. Ooi, Superhydrophobic PVDF/TiO2-SiO2 membrane with hierarchical roughness in membrane distillation for water recovery from phenolic rich solution containing surfactant. Chin. J. Polym. Sci. (Engl. Ed.) **37**(6), 609–616 (2019). https://doi.org/10.1007/s10118-019-2235-y

N. Ismail, M. Essalhi, M. Rahmati, Z. Cui, M. Khayet, N. Tavajohi, Experimental and theoretical studies on the formation of pure β-phase polymorphs during fabrication of polyvinylidene fluoride membranes by cyclic carbonate solvents. Green Chem. **23**(5), 2130–2147 (2021). https://doi.org/10.1039/D1GC00122A

N. Li, Hduo Chen, Yze Lu, Mchao Zhu, Zxia Hu, Swen Chen, R.J. Zeng, Nanoscale zero-valent iron-modified PVDF membrane prepared by a simple filter-press coating method can robustly remove 2-chlorophenol from wastewater. Chem. Eng. J. **416**, 127701 (2021). https://doi.org/10.1016/J.CEJ.2020.127701

N. Prabhakar, A.M. Isloor, M. Padaki, A. Fauzi Ismail, Fabrication of TiO2@ZIF-67 metal organic framework composite incorporated PVDF membranes for the removal of hazardous reactive black 5 and Congo red dyes from contaminated water. Chem. Eng. J. **498**, 155270 (2024). https://doi.org/10.1016/j.cej.2024.155270

N.S. Fuzil, N.H. Othman, N.H. Alias, F. Marpani, M.S. Mat Shayuti, M.Z. Shahruddin, M.R. Mohd Razlan, N. Abd Rahman, W.J. Lau, M.H.D. Othman, A.F. Ismail, T.D. Kusworo, A. Ul-Hamid, MoS2-TiO2 coated PVDF-based hollow fiber membranes for permeate flux enhancement in membrane distillation. J. Environ. Chem. Eng. **11**(3), 109866 (2023). https://doi.org/10.1016/j.jece.2023.109866

O. Wilhelmsson, S. Bijelovic, M. Lindquist, B. André, U. Wiklund, P. Svedlindh, U. Jansson, Deposition and characterization of magnetic Ti-Fe-C nanocomposite thin films. Thin Solid Films. **518**(10), 2607–2616 (2010). https://doi.org/10.1016/j.tsf.2009.07.195

P. Awasthi, R.S. Bangari, N. Sinha, PVDF/BNNSs nanocomposite membrane for simultaneous removal of tetracycline and ofloxacin from water. J. Mol. Liq. **370**, 120970 (2023). https://doi.org/10.1016/j.molliq.2022.120970

P.L.N. Khui, M.R. Rahman, KAbinM. Said, M. Namakka, M. Shahabuddin, M.S.M. Al-Saleem, J.Y. Al-Humaidi, M.M. Rahman, Enhanced flux and surface modification of PVDF hollow fiber membranes using bamboo cellulose/PVA composite coatings. Polym. Bull. (2025). https://doi.org/10.1007/s00289-025-06023-8

P. Mensah, T. Osobamiro, P. Ramasami, Simultaneous remediation of polycyclic aromatic hydrocarbon and heavy metals in wastewater with zerovalent iron-titanium oxide nanoparticles (ZVI-TiO2). Phys. Sci. Rev. **8**(12), 5185–5194 (2023). https://doi.org/10.1515/psr-2021-0213

P. Yu, H. Yu, Q. Sun, B. Ma, Filter paper supported nZVI for continuous treatment of simulated dyeing wastewater. Sci. Rep. **9**(1), 1–8 (2019). https://doi.org/10.1038/s41598-019-47863-5

Q. Chen, Z. Luo, C. Hills, G. Xue, M. Tyrer, Precipitation of heavy metals from wastewater using simulated flue gas: sequent additions of fly ash, lime and carbon dioxide. Water Res. **43**(10), 2605–2614 (2009). https://doi.org/10.1016/j.watres.2009.03.007

Q. Jing, W. You, S. Qiao, Y. Ma, Z. Ren, Comprehensive understanding of adsorption and reduction on 2,4-DCP and Cr(VI) removal process by NZVI-rGO: performance and mechanism. J. Water Process Eng. **51**, 103413 (2023). https://doi.org/10.1016/j.jwpe.2022.103413

Q. Li, H. Wang, Z. Chen, X. He, Y. Liu, M. Qiu, X. Wang, Adsorption-reduction strategy of U(VI) on NZVI-supported zeolite composites via batch, visual and XPS techniques. J. Mol. Liq. **339**, 116719 (2021). https://doi.org/10.1016/j.molliq.2021.116719

Q. Zhao, H. Yang, L. Tong, R. Jin, Pollution characteristics of pyrite surface in cyanide tailings by PCA-assisted ToF-SIMS and their correlation with the contact angle. Jom **76**(1), 547–557 (2023). https://doi.org/10.1007/s11837-023-06143-4

R. Fu, Y. Yang, Z. Xu, X. Zhang, X. Guo, D. Bi, The removal of chromium (VI) and lead (II) from groundwater using sepiolite-supported nanoscale zero-valent iron (S-NZVI). Chemosphere **138**, 726–734 (2015). https://doi.org/10.1016/j.chemosphere.2015.07.051

R. Gayatri, E. Yuliwati, A. Noor Syimir Fizal, M. Zulhilmi Zailani, J. Jaafar, M. Zulkifli, W. Taweepreda, A. Naim Ahmad Yahaya, Effect of TiO2 concentration in PVDF-TiO2-PVP mixed matrix membrane performance using ultrafiltration process. Mater. Today Proc. **96**, 1–5 (2024). https://doi.org/10.1016/J.MATPR.2023.08.016

R. Liu, H. Jiang, P. Li, J. Yin, Z. Xu, X. Chen, J. Cheng, S. Gu, R. Lyu, Degradation mechanism of antibiotics by flower-like Bi2S3 sensitized anatase/rutile TiO2 coupled with SiO2 photonic crystals. J. Water Process Eng. **58**(February), 104827 (2024). https://doi.org/10.1016/j.jwpe.2024.104827

R. Rahman, A. James, A. Mohamed, (2024b). *Materials Advances polyvinylidene fluoride (PVDF) nanocomposite membrane for wastewater treatment by a photocatalytic process*. https://doi.org/10.1039/d4ma00716f

R. Razavi, A. Shakeri, H. Salehi, A novel thin film nanocomposite forward osmosis membrane modified with zwitterionic GO-g-PSBMA with high fouling resistance and heavy metal ions rejection. J. Environ. Chem. Eng. **13**(1), 115308 (2025). https://doi.org/10.1016/j.jece.2025.115308

R. Zhang, R. Napolano, B. Xi, A.M. Salazar, Q. Shi, Y. Zhao, X. Meng, Mechanistic insights into Cr(VI) removal by a combination of zero-valent iron and pyrite. Chemosphere **330**, 138693 (2023). https://doi.org/10.1016/j.chemosphere.2023.138693

S. Acarer-Arat, M. Tüfekci, İ Pir, N. Tüfekci, Nanocellulose in polyvinylidene fluoride (PVDF) membranes: assessing reinforcement impact and modelling techniques. J. Environ. Chem. Eng. **12**(6), 114749 (2024). https://doi.org/10.1016/j.jece.2024.114749

S. Astuti, Arief, M. Muldarisnur, Zulhadjri, S.R.A. Usna, (2023). Enhancement in photoluminescence performance of carbon-based Fe3O4@ZnO–C nanocomposites. *Vacuum*, *211*(December 2022), 111935. https://doi.org/10.1016/j.vacuum.2023.111935

S. Aziz, A. Abdel-Karim, Dual-functional ultrafiltration biocatalytic membrane containing laccase/ nanoparticle for removal of pollutants: a review. Environ. Nanotechnol. Monit. Manag. **20**, 100852 (2023). https://doi.org/10.1016/j.enmm.2023.100852

S.H. Ammar, A. Ibrahim Elaibi, I. Sh. Mohammed, Core/shell Fe3O4@Al2O3-PMo magnetic nanocatalyst for photocatalytic degradation of organic pollutants in an internal loop airlift reactor. J. Water Process Eng. **37**(June), 101240 (2020). https://doi.org/10.1016/j.jwpe.2020.101240

S. Jain, J. Shah, N.S. Negi, C. Sharma, R.K. Kotnala, Significance of interface barrier at electrode of hematite hydroelectric cell for generating ecopower by water splitting. Int. J. Energy Res. **43**(9), 4743–4755 (2019). https://doi.org/10.1002/er.4613

S.K. Krishnan, K. Subbiah, V. Chandrapragasam, K. Subramanian, Comparison of membrane immobilized zero-valent iron nanoparticles for RED ME4BL azodye degradation. J. Appl. Nat. Sci. **15**(2), 818–825 (2023). https://doi.org/10.31018/jans.v15i2.4253

S. Koçak Soylu, O.S. Özdemir, M. Asiltürk, İ. Atmaca, Thermal and optical characteristics of TiO2@SiO2, Fe3O4@SiO2, and ZnO@SiO2 core–shell nanoparticles and their water-based nanofluids. Int. J. Thermophys. (2025b). https://doi.org/10.1007/s10765-025-03558-w

S. Koçak Soylu, O.S. Özdemir, M. Asiltürk, İ. Atmaca, Thermal and optical characteristics of TiO2@SiO2, Fe3O4@SiO2, and ZnO@SiO2 Core–Shell nanoparticles and their Water-Based nanofluids. Int. J. Thermophys. (Vol. **46** (2025a). https://doi.org/10.1007/s10765-025-03558-w

S. Madan, R. Shaw, S. Tiwari, S.K. Tiwari, Enhancing corrosion stability and shelf life of nanoscale zero-valent iron via encapsulation in porous Ze-TiO2 matrix: an interface for simultaneous oxidation and adsorption of As(III). Colloids Surf. A Physicochem. Eng. Asp. **607**(June), 125381 (2020). https://doi.org/10.1016/j.colsurfa.2020.125381

S.M. Botsa, (2025). Reduced graphene oxide - assisted TiO 2 - Fe 2 O 3 ternary nanocomposite for efficient visible - light driven photocatalysis of nitrobenzene and dye pollutants

S. Reghunath, D. Pinheiro, S.D. Kr, A review of hierarchical nanostructures of TiO2: advances and applications. Appl. Surf. Sci. Adv. (2021). https://doi.org/10.1016/j.apsadv.2021.100063

S. Xie, J. Su, J. Zhao, H. Yang, H. Qian, An amorphous zero-valent iron decorated by Fe3O4 significantly improves the Fenton-like reaction. J. Alloys Compd. **929**, 167306 (2022). https://doi.org/10.1016/j.jallcom.2022.167306

S.Z. Iron, N.A. Green, B.A. Lajayer, (2023). *Pb (II) Removal from Aqueous Solutions by Adsorption on. Ii*, 1–23

T. Iqbal, R. Sahrash, A. Siddiqa, S. Afsheen, M.B. Tahir, M.I. Khan, K.N. Riaz, G. Nabi, M. Fahad, M. Sharif, M. Abrar, Preparation and characterization of polyvinylidene fluoride/1-butyl-3-methylimidazolium bromide-based ionogel membranes for desalination applications. Int. J. Environ. Sci. Technol. **16**(11), 7081–7092 (2019). https://doi.org/10.1007/s13762-019-02207-8

T.M.H. Le, R. Wang, S. Sairiam, Self-protecting PVDF-PDA-TiO2 membranes towards highly efficient and prolonged dye wastewater treatment by photocatalytic membranes. J. Membr. Sci. **683**(March), 121789 (2023). https://doi.org/10.1016/j.memsci.2023.121789

T. Munawar, F. Mukhtar, K.M. Batoo, A. Mazhar, M.S. Nadeem, S. Hussain, A.W. Rabbani, U. Ali Akbar, A.S. Hakeem, F. Iqbal, Sunlight-activated Mo-doped La2CuO4/rGO perovskite oxide nanocomposite for photocatalytic treatment of diverse dyes pollutant. Materials Science and Engineering: B **304**, 117355 (2024). https://doi.org/10.1016/j.mseb.2024.117355

T.N. Moja, N. Bunekar, S. Mojaki, S.B. Mishra, T.Y. Tsai, S.S. Hwang, A.K. Mishra, Polypropylene–Polypropylene-grafted-maleic anhydride–Montmorillonite clay nanocomposites for Pb(II) removal. J. Inorg. Organomet. Polym. Mater. **28**(6), 2799–2811 (2018). https://doi.org/10.1007/s10904-018-0936-2

V.M. Hadkar, C.I. Selvaraj, Bio-inspired Ag3PO4-ZnO nanocomposites: investigation of its antioxidant, anticancer activity and photocatalytic degradation of methylene blue dye. J. Inorg. Organomet. Polym. Mater. (2025). https://doi.org/10.1007/s10904-025-03895-1

V. Subha, S. Gowri, R. Kayalvizhi, T. Kamatchi, A novel NiMn2O4@rGO nanocomposite as a photocatalytic application against organic pollutants. J. Inorg. Organomet. Polym. Mater. **35**(10), 8759–8773 (2025). https://doi.org/10.1007/s10904-025-03787-4

W. Biao, N. Awanis Hashim, M. F. Bin. Rabuni, O. Lide, A. Ullah, An innovative strategy for polyester microplastic fiber elimination from laundry wastewater via coupled separation and degradation using TiO2-based photocatalytic membrane reactor. Sep. Purif. Technol. **356**, 129929 (2025). https://doi.org/10.1016/j.seppur.2024.129929

W. Li, R. Liang, A. Hu, Z. Huang, Y.N. Zhou, Generation of oxygen vacancies in visible light activated one-dimensional iodine TiO2 photocatalysts. RSC Adv. **4**(70), 36959–36966 (2014). https://doi.org/10.1039/c4ra04768k

World Health Organization. (2003). Iron in drinking-water. WHO Guidelines for drinking-water quality. *Who/Sde/Wsh/03.04/08*, *2*, 4.

W.P. Hsieh, J.R. Pan, C. Huang, Y.C. Su, Y.J. Juang, Enhance the photocatalytic activity for the degradation of organic contaminants in water by incorporating TiO2 with zero-valent iron. Sci. Total Environ. **408**(3), 672–679 (2010). https://doi.org/10.1016/j.scitotenv.2009.07.038

W.S. Chai, J.Y. Cheun, P.S. Kumar, M. Mubashir, Z. Majeed, F. Banat, S.H. Ho, P.L. Show, A review on conventional and novel materials towards heavy metal adsorption in wastewater treatment application. J. Clean. Prod. **296**, 126589 (2021). https://doi.org/10.1016/j.jclepro.2021.126589

W. Sun, J. Liu, H. Chu, B. Dong, Pretreatment and membrane hydrophilic modification to reduce membrane fouling. Membranes **3**(3), 226–241 (2013). https://doi.org/10.3390/membranes3030226

W. Zhang, G. Wu, H. Zeng, Z. Li, W. Wu, H. Jiang, W. Zhang, R. Wu, Y. Huang, Z. Lei, The preparation, structural design and application of electroactive poly (vinylidene fluoride) - based materials for wearable sensors and human energy harvesters. Polymers **15**(13), 2766 (2023). https://doi.org/10.3390/polym15132766

X. Li, M. Gao, Y. Huo, H. Liu, J. Li, T. Huang, R. Ye, W. Li, Impacts of shell structure on nitrate-reduction activity and air stability of nanoscale zero-valent iron. Environ. Sci. Pollut. Res. **29**(53), 80683–80692 (2022). https://doi.org/10.1007/s11356-022-21460-y

X. Yu, L. Jiajun, Y. Xianglin, Z. Feng, L. Yongjun, L. Junbo, Preparation of graphdiyne-doped TiO2/SiO2 composite for enhanced photocatalytic activity. J. Nanopart. Res. (2020). https://doi.org/10.1007/s11051-020-05097-x

X. Zhang, K. Zhang, Y. Shi, H. Xiang, W. Yang, F. Zhao, Surface engineering of multifunctional nanostructured adsorbents for enhanced wastewater treatment: a review. Sci. Total Environ. **920**, 170951 (2024). https://doi.org/10.1016/j.scitotenv.2024.170951

Y. Bai, S. Zhang, K. Zhang, J. Li, J. Zhang, M. Hao, H. Tao, The nitro-modified NO2-MIL-53(Fe) activating persulfate for the efficient degradation of tetracycline: performance and mechanism. J. Inorg. Organomet. Polym. Mater. **53**(2), 9525–9542 (2025). https://doi.org/10.1007/s10904-025-03848-8

Y.C.G. Kwan, G.M. Ng, C.H.A. Huan, Identification of functional groups and determination of carboxyl formation temperature in graphene oxide using the XPS O 1s spectrum. Thin Solid Films **590**, 40–48 (2015). https://doi.org/10.1016/j.tsf.2015.07.051

Y. Chen, X.F. Zhang, A.J. Wang, Q.L. Zhang, H. Huang, J.J. Feng, Ultrafine Fe3C nanoparticles embedded in N-doped graphitic carbon sheets for simultaneous determination of ascorbic acid, dopamine, uric acid and xanthine. Microchim. Acta (2019). https://doi.org/10.1007/s00604-019-3769-y

Y. Ezaier, A. Hader, A. Latif, M.E. Khan, W. Ali, S.K. Ali, A.H. Bashiri, W. Zakri, M. Yusuf, N. Rajamohan, H. Ibrahim, Solving the fouling mechanisms in composite membranes for water purification: an advance approach. Environ. Res. **250**, 118487 (2024). https://doi.org/10.1016/j.envres.2024.118487

Y. Geng, H. Tang, Y. Zhang, J. Cao, X. Li, S. Wang, Y. Liu, Y. Gong, Degradation of tetracycline by MIL-88B(Fe)@CuS composite efficiently activated peroxydisulfate. J. Inorg. Organomet. Polym. Mater. (2025). https://doi.org/10.1007/s10904-025-03826-0

Y. Huang, W. Zhang, M. Zhang, X. Zhang, Y. Zhao, Hydroxyl-functionalized TiO2@SiO2@Ni/nZVI nanocomposites fabrication, characterization and enhanced simultaneous visible light photocatalytic oxidation and adsorption of arsenite. Chem. Eng. J. **338**, 369–382 (2018). https://doi.org/10.1016/j.cej.2018.01.019

Y.P. Sun, Xqin Li, J. Cao, Wxian Zhang, H.P. Wang, Characterization of zero-valent iron nanoparticles. Adv. Colloid Interface Sci. **120**(1–3), 47–56 (2006). https://doi.org/10.1016/j.cis.2006.03.001

Z. Hejri, M. Hejri, M. Omidvar, S. Morshedi, Synthesis of TiO2/nZVI nanocomposite for nitrate removal from aqueous solution. Int. J. Ind. Chem. **10**(3), 225–236 (2019). https://doi.org/10.1007/s40090-019-0186-3

Z. Kuspanov, A. Serik, A. Tattibay, A. Baratov, U. Abdikarimova, M. Bissenova, M. Yeleyov, S. Sakhiyev, C. Daulbayev, Investigating and correlating the photocatalytic activity of synthesised strontium titanate nanopowder with calcination temperature. Environ. Technol. Innov. **36**, 103852 (2024). https://doi.org/10.1016/J.ETI.2024.103852

Z. Razmara, M.M. Rosli, I.A. Razak, Single-crystal structure feature of a novel water-soluble Cu(II) complex as a heterogeneous catalyst for oxidation reactions. J. Inorg. Organomet. Polym. Mater. (2025). https://doi.org/10.1007/s10904-025-03847-9

Z. Wang, Z. Tan, H. Li, S. Yuan, Y. Zhang, Y. Dong, Direct current electrochemical method for removal and recovery of heavy metals from water using straw biochar electrode. J. Clean. Prod. **339**, 130746 (2022). https://doi.org/10.1016/j.jclepro.2022.130746

Authors and Affiliations

Murtala Namakka[1,2] · **Md. Rezaur Rahman**[1] · **Khairul Anwar Bin Mohamed Said**[1] · **Bavya Devi Karuppasamy**[3] · **Aliyu Abubakar Shehu**[4]

✉ Murtala Namakka
abuhuzaifah33@yahoo.com

✉ Md. Rezaur Rahman
rmrezaur@unimas.my

[1] Department of Chemical Engineering and Energy Sustainability, Universiti Malaysia Sarawak, Kota Samarahan, Malaysia

[2] Department of Chemical Engineering, Ahmadu Bello University, Zaria, Nigeria

[3] Centre for Research and Development, KPR Institute of Engineering and Technology, Tamilnadu, India

[4] Usman Dan Fodio University, Sokoto, Nigeria